

The FLASHES Survey I: Integral Field Spectroscopy of the CGM around 48 $z \simeq 2.3 - 3.1$ QSOs

DONAL B. O’SULLIVAN,¹ CHRISTOPHER MARTIN,¹ MATEUSZ MATUSZEWSKI,¹ KERI HOADLEY,¹ ERIKA HAMDEN,¹
JAMES D. NEILL,¹ ZEREN LIN,¹ AND PRACHI PARIHAR¹

¹*California Institute of Technology*

ABSTRACT

We present the pilot study component of the Fluorescent Lyman-Alpha Structures in High- z Environments (FLASHES) Survey; the largest integral-field spectroscopy survey to date of the circumgalactic medium at $z = 2.3 - 3.1$. We observed 48 quasar fields between 2015 and 2018 with the Palomar Cosmic Web Imager (Matuszewski et al. (2010)). Extended HI Lyman- α emission is discovered around 42/48 of the observed quasars, ranging in projected, flux-weighted radius from 21 – 71 proper kiloparsecs (pkpc), with 26 nebulae exceeding 100 pkpc in effective diameter. The circularly averaged surface brightness radial profile peaks at a maximum of 1×10^{-17} erg s⁻¹ cm⁻² arcsec⁻² (2×10^{-15} erg s⁻¹ cm⁻² arcsec⁻² adjusted for cosmological dimming) and luminosities range from 1.9×10^{43} erg s⁻¹ to -14.1×10^{43} erg s⁻¹. The emission appears to have a highly eccentric morphology and a maximum covering factor of 50% (60% for giant nebulae). On average, the nebular spectra are red-shifted with respect to both the systemic redshift and Ly α peak of the quasar spectrum. The integrated spectra of the nebulae mostly have single or double-peaked line shapes with global dispersions ranging from 167 km s⁻¹ to 690 km s⁻¹, though the individual (Gaussian) components of lines with complex shapes mostly appear to have dispersions ≤ 400 km s⁻¹, and the flux-weighted velocity centroids of the lines vary by thousands of km s⁻¹ with respect to the systemic QSO redshifts. Finally, the root-mean-square velocities of the nebulae are found to be consistent with gravitational motions expected in dark matter halos of mass $M_h \simeq 10^{12.5} M_\odot$. We compare these results to existing surveys at both higher and lower redshift.

1. INTRODUCTION

To understand the evolution of galaxies and their properties, it is critical to understand their environments. Our current picture of galaxy formation takes place in a universe dominated by cold dark matter (Blumenthal et al. 1984). In this picture, dark matter structures collapse in a hierarchical manner, dragging with them the baryonic material that eventually forms and fuels galaxies. A key element of this framework is the interplay between galaxies and their environments; galaxies form and evolve through a series of interactions with both the circumgalactic and intergalactic medium (CGM and IGM; e.g., Bond et al. 1996; Fukugita et al. 1998). A long history of accretion, outflows and merger events underlies the properties of galaxies that we observe today (e.g., Kereš et al. 2005; Dekel et al. 2009;

Fumagalli et al. 2011; Correa et al. 2015).

With the development of highly sensitive integral field spectrographs, there is now the opportunity to contribute substantial direct observational evidence to the discussion around high-redshift galaxy environments, which has so far taken place largely in the realms of theory and simulation. The sensitivity, spatial resolution and spectral flexibility of these new instruments enable exploratory surveys which map the density, morphology, composition and kinematics of the CGM. Several integral-field spectroscopy (IFS) studies of individual objects or small samples have already produced fascinating insights into galactic environments at high redshift ($z \gtrsim 2$), such as extended emission line regions from quasar feedback or in-falling material (e.g., Christensen et al. (2006)), giant cosmic web filaments connected to quasars or Lyman-Alpha Blobs (e.g., Martin et al. (2014a,b)), and kinematic signatures remarkably consistent with giant, rotating disks embedded in the CGM (e.g., Martin et al. (2015, 2016)). While individual case studies and small samples can provide detailed

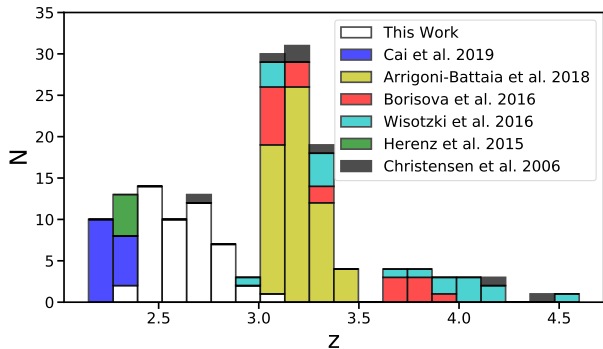


Figure 1. IFS surveys of extended emission around high redshift galaxies. Surveys are shown as stacked histograms representing the number of targets in each.

environmental diagnostics, they tend to focus on the brightest (or otherwise notable) quasars. Most studies thus far have characterized nebular emission using the HI Lyman-alpha ($\text{Ly}\alpha$) transition, which outshines other emission lines by an order of magnitude or more in the diffuse CGM/IGM (Bertone & Schaye 2012; Bertone et al. 2013).

However, to fully characterize the morphology, composition and dynamics of the CGM, large samples with deep multi-wavelength observations are needed. Recently, teams using the Multi-Unit Spectroscopic Explorer (MUSE) on the Very Large Telescope (Caillier et al. 2014) have produced surveys of $\text{Ly}\alpha$ emission around quasars and galaxies at $z \gtrsim 3$ with sample sizes on the order of tens of targets. Borisova et al. (2016) (hereafter B16) studied 17 bright radio-quiet quasars (and 2 radio-loud) at $z \sim 3.5$, finding ubiquitous “giant” $\text{Ly}\alpha$ nebulae on scales larger than 100 pkpc, with clear asymmetries and a circularly-averaged radial profile following power laws. Arrigoni-Battaia et al. (2018) (hereafter A18) studied 61 QSOs with a median redshift of 3.17, finding $\text{Ly}\alpha$ nebulae extending on the order of tens of kpc around their quasars. The nebulae they discover have some spread in their degree of spatial symmetry, and they find their radial profiles are best fit by an exponential profile with a scale length $r_H \sim 15$ pkpc. They compare this to a narrow-band study at $z \sim 2$ (Arrigoni-Battaia et al. 2016), but with the actual centroid of $\text{Ly}\alpha$ emission varying by thousands of km s^{-1} from systemic QSO redshifts, it is not clear how reliable narrow-band imaging is without prior knowledge of the emission wavelength. Wisotzki et al. (2016) performed an ultra-deep exposure of the *Hubble* Deep Field South with MUSE, reaching a (1σ) limiting surface brightness of $1 \times 10^{-19} \text{erg s}^{-1} \text{cm}^{-2} \text{arcsec}^{-2}$. They report detections of extended $\text{Ly}\alpha$ halos around

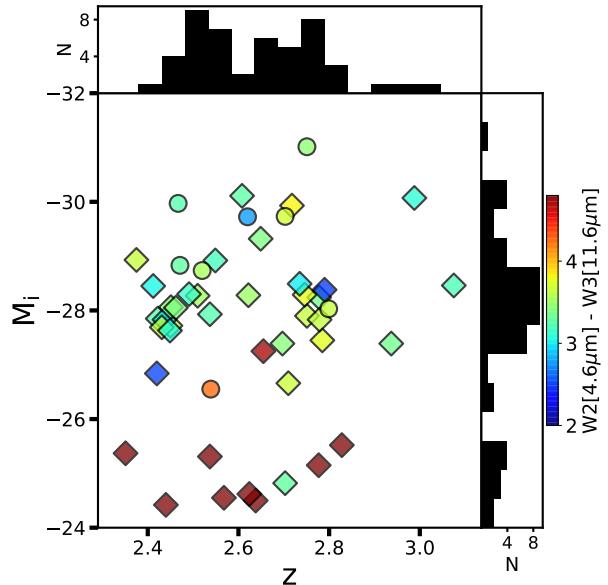


Figure 2. The FLASHES pilot sample in redshift (z) vs. absolute i-band magnitude (M_i). Circles indicate targets for which the value of M_i is estimated from the given apparent magnitude, while diamonds indicate those for which a value of M_i was provided in the SDSS DR12Q. The colorbar indicates the WISE infrared color $W2[4.6\mu\text{m}] - W3[11.6\mu\text{m}]$ color.

21 of the 26 total $z = 3 - 6$ galaxies in their sample, on spatial scales of $R_{\perp} \sim \mathcal{O}(10 \text{ pkpc})$. The remaining 5 non-detections represent the faintest galaxies in the sample, and thus they are thought to be a matter of insufficient Signal-to-Noise (S/N), making the overall result consistent with the ubiquitous $\text{Ly}\alpha$ halos reported in B16. More recently, Cai et al. (2019) observed 16 QSOs with redshifts $z = 2.1 - 2.3$ using the Keck Cosmic Web Imager (Morrissey et al. 2018) (KCWI) and report extended emission around all of them, although 2/16 of the nebulae are reported to have projected sizes smaller than 50 pkpc. The authors find that the nebulae are more asymmetric and lower in surface brightness than the $z > 3$ MUSE studies.

We have utilized the Palomar Cosmic Web Imager (PCWI - Matuszewski et al. (2010)) to conduct a pilot study of the gaseous environments of quasars spanning a redshift range of $z = 2.3 - 3.1$, filling a gap in existing observations (see Figure 1). This survey, which we call FLASHES (Fluorescent Lyman-Alpha Structures in High- z Environments), consists of a broad pilot survey component, presented in this paper, and follow-up deep survey, to be presented in a future paper. The pilot survey aims to map $\text{Ly}\alpha$ emission from the CGM around the full sample of 48 quasars at redshifts $2.3 \leq z \leq 3.1$ to a limiting (2σ) surface-brightness $\sim 5 \times 10^{-18} \text{erg}$

$\text{s}^{-1}\text{cm}^{-2}\text{arcsec}^{-2}$. Based on existing observational work (e.g., AB18, BS16), this is expected to be sufficient to map CGM Ly α emission within a 50 – 100 proper kiloparsecs (pkpc) of the quasars, and enable us to constrain the morphology and kinematics of the CGM in this redshift range. In addition, we search for the presence of the gaseous filaments that are theorized to feed gas from the cosmic web into dark matter halos. Recent observations have offered tantalizing direct evidence supporting cold-flow accretion from multiple filaments forming ‘cold inflow disks’ (Martin et al. 2015, 2016, 2019). A larger sample of observations will allow us to test the validity of such models and their utility in constraining the gas dynamics associated with cold-flow accretion. A subset of these targets will be followed up with deep KCWI exposures for the latter component of the survey, targeting Ly α emission at surface brightness levels an order of magnitude fainter than in the pilot survey, as well as targeting emission from metals such as $\lambda\text{CIV}1549$ and $\lambda\text{HeII}1640$ which probe the multi-phase structure of the CGM.

In this paper, we focus exclusively on the FLASHES pilot survey. In Section 2 we describe the survey methodology, target selection, and choice of observables. In Section 3 we present a summary of the observations and data. In Section 4 we describe the data reduction with the standard PCWI pipeline and a newly developed Python3 package, ‘CWITools’. In Section 5 we describe the data analysis required to extract and characterize the nebular emission. In Section 6 we present the core observational results: emission maps, kinematic maps, spectra, symmetries and radial profiles. Finally, in Section 7 we discuss the implication of our results, sensitivity limits, and comparisons to existing work, before summarizing our findings in Section 8. For calculations of the luminosity distance and physical plate scales (pkpc per pixel) throughout the paper, we use a ΛCDM cosmology with $H_0 = 70\text{kms}^{-1}\text{Mpc}^{-1}$, $\Omega_b = 0.3$ and $\Omega_\Lambda = 0.7$.

Table 1. Summary of FLASHES Pilot Observations

ID	Target Name	Coordinates	z_{QSO}	M_i	Seeing	Cloud Cover	Humidity	Exp
		hh:mm:ss.ss \pm dd:mm:ss.ss						
1	SDSS0103+1316 ^a	01:03:11.27 +13:16:17.70	2.705	-29.93	1.9	CLR	49	56
2	SDSS1112+1521	11:12:52.45 +15:21:23.50	2.790	-28.38	1.1	CLR	25	60
3	SDSS0834+1238	08:34:08.63 +12:38:36.54	2.746	-28.29	1	CLR-PC	40	60
4	HS1700+6416 ^a	17:01:01.00 +64:12:09.10	2.737	-31.01	1.1-1.5	CLR	20-30	222
5	SDSS1011+2941 ^a	10:11:56.00 +29:41:42.00	2.640	-30.11	1.1-1.5	CLR	35	60
6	SDSS0837+1459	08:37:12.89 +14:59:17.38	2.515	-28.27	2	CLR	35	48
7	SDSS0735+3744	07:35:35.44 +37:44:50.42	2.750	-27.90	1.3	CLR	20	60
8	SDSS0958+4703	09:58:45.42 +47:03:24.43	2.491	-28.30	2.1	CLR	56	60
9	SDSS0057+0346	00:57:37.78 +03:46:45.03	2.445	-27.83	2.1	CLR	56	60
10	SDSS2241+1225	22:41:45.11 +12:25:57.24	2.632	-28.28	1.6-1.9	CLR	50	60
11	SDSS0214+1912 ^a	02:14:29.71 +19:12:37.40	2.471	-28.83	1.5-2.0	CLR-PC	30-55	70
12	SDSS2328+0443 ^{c,b}	23:28:28.48 +04:43:46.84	2.568	-24.55	1.6-1.9	CLR-PC	50	60
13	SDSS0108+1635 ^a	01:08:06.40 +16:35:50.00	2.644	-29.32	1.6	PC	50	70
14	SDSS0851+3148 ^c	08:51:24.79 +31:48:55.72	2.638	-24.50	1.0 - 1.5	CLR-PC	73	60
15	SDSS0132+3326 ^d	01:32:44.60 +33:26:55.42	2.420	-26.84	1.4	CLR-F	40	60
16	SDSS2338+1504 ^e	23:38:23.16 +15:04:45.22	2.419	-28.45	1.5-2.0	CLR-PC	30-55	56
17	SDSS2339+1901 ^b	23:39:44.60 +19:01:52.00	2.620	-29.72	1.5-1.9	CLR-PC	25-49	60
18	SDSS0015+2927	00:15:53.14 +29:27:21.45	3.075	-28.46	1.3	CLR	20	60
19	SDSS0730+4340	07:30:02.80 +43:40:03.04	2.937	-27.39	1.8	CLR	14	60

Table 1 *continued*

Table 1 (*continued*)

ID	Target Name	Coordinates	z_{QSO}	M_i	Seeing	Cloud Cover	Humidity	Exp
		hh:mm:ss.ss \pm dd:mm:ss.ss		AB mag	arcsec		%	min
20	SDSS0006+1614	00:06:39.47 +16:14:59.30	2.440	-27.85	1.6-2.0	TC	35-50	60
21	SDSS1428+2336	14:28:10.96 +23:36:40.21	2.789	-27.83	1.0-1.4	CLR-F	40-57	60
22	SDSS0300+0222 ^b	03:00:46.02 +02:22:45.24	2.524	-28.73	2	CLR	35	68
23	SDSS0639+3819	06:39:01.60 +38:19:15.24	2.539	-26.55	1.3	CLR	20	60
24	SDSS0013+1630 ^d	00:13:55.86 +16:30:51.78	2.591	-27.93	1.6	CLR	14	60
25	SDSS1218+2414	12:18:10.98 +24:14:10.90	2.381	-28.93	1.5	CLR-PC	35	40
26	SDSS0205+1902 ^b	02:05:27.51 +19:02:29.10	2.703	-29.73	1.6	TC	50	70
27	SDSS0118+1950	01:18:39.93 +19:50:27.86	2.778	-28.24	1.1	CLR	15	60
28	SDSS0822+1626	08:22:00.22 +16:26:52.87	2.475	-28.06	1.4	CLR-PC	63	60
29	SDSS2340+2418 ^{c,d}	23:40:39.74 +24:18:59.15	2.348	-25.37	1.4	CLR-F	40	60
30	SDSS0753+4030	07:53:26.11 +30:40:38.63	2.930	-28.72	1.5	TC	25	60
31	SDSS1626+4858 ^e	16:25:59.89 +48:58:17.49	2.701	-28.49	1.1	CLR-PC	25	54
32	SDSS0321+4132	03:21:08.45 +41:32:20.86	2.446	-29.97	1.5-2.0	TC	30	70
33	SDSS0303+3838	03:03:09.16 +38:38:57.20	2.799	-28.03	1.1	CLR	15	60
34	SDSS2151+0921	21:51:55.30 +09:21:14.07	2.444	-27.63	1.5-2.0	CLR-PC	30-55	56
35	SDSS1002+2008	10:02:55.43 +20:08:02.56	2.660	-27.25	1.0 - 1.3	CLR	55 - 73	60
36	SDSS0126+1559	01:26:36.12 +15:59:29.94	2.694	-27.39	1.5	PC	27	64
37	SDSS0012+3344	00:12:15.26 +33:44:00.33	2.450	-27.72	2	CLR-PC	35	60
38	SDSS0144+0838	01:44:14.08 +08:38:20.40	2.440	-27.69	1.5-2.0	TC	25-55	60
39	SDSS1532+3059	15:32:58.24 +30:59:06.59	2.580	-28.92	1.0-1.5	CLR-PC	35	40
40	SDSS2259+2326	22:59:04.02 +23:26:43.91	2.462	-28.05	1.3	CLR	10	60
41	SDSS1552+1757	15:52:00.50 +17:57:22.70	2.703	-24.82	1.0-1.3	CLR	55-73	80
42	SDSS1258+2123 ^c	12:58:11.25 +21:23:59.70	2.624	-24.62	1.3	CLR	73	70
43	SDSS0211+3117	02:11:39.25 +31:17:24.67	2.785	-27.45	1.6-1.9	CLR-PC	49-55	60
44	SDSS2234+2637 ^c	22:34:53.07 +26:37:25.00	2.777	-25.15	1.5	CLR-PC	27	60
45	SDSS0137+2405 ^c	01:37:58.65 +24:05:41.01	2.440	-24.42	1.5-2.0	CLR-PC	30-55	60
46	SDSS0107+1104 ^{c,d}	01:07:14.66 +11:04:46.10	2.542	-25.31	1.4	CLR	14	60
47	SDSS2350+3135 ^c	23:50:36.46 +31:35:05.02	2.828	-25.52	1.5	CLR	43	60
48	SDSS0041+1925	00:41:09.83 +19:25:19.85	2.702	-26.66	1.5	TC	27	60

NOTE— z_{QSO} , the QSO’s systemic redshift, is from DR12Q where available and SDSS or 2MASS elsewhere. M_i , the QSO’s absolute i-band magnitude, is taken from DR12Q where given and derived using the luminosity distance elsewhere. For cloud cover: CLR - Clear, PC - Patchy Clouds, TC-Thin Cirrus, F-Fog.

^aLiterature target

^bTarget selected from SIMBAD to fill observing schedule

^cDust-obscured targets, indicated by $W2 - W3$ WISE color.

^dObserved without Nod-and-Shuffle technique.

^eRadio-loud QSO

2. SURVEY METHODOLOGY

2.1. Choice of Observables

At a redshift of $z = 2$, Bertone et al. (2013) estimate that 80% of the energy emitted by the diffuse material of the CGM/IGM is carried by emission lines, with the remaining 20% in continuum emission. The Hydrogen

Lyman series - and primarily $\text{Ly}\alpha$ - is the main contributor to this, carrying 20% of the line emission energy budget. Metal lines serve as better tracers for a wider range of over-densities or temperatures. They are typically an order of magnitude fainter than $\text{Ly}\alpha$ and depend strongly on gas metallicity and phase (Bertone & Schaye 2012). The ubiquity and brightness of $\text{Ly}\alpha$ make it a clear choice for the pilot survey’s goal of detecting and mapping the cool-warm phase of the CGM. With $\text{Ly}\alpha$, we can constrain the morphology, density and baryonic mass of detected nebulae. Targets of interest can then be followed-up in the deep study component of the survey, targeting metal lines such as HeII and CIV, in order to get a more complete picture of the multi-phase CGM.

2.2. Target Selection

The FLASHES sample is primarily selected from SDSS DR12Q - the QSO Catalog from the 12th Data Release of the Sloan Digital Sky Survey (Alam & et al. 2015). Targets were chosen within the redshift range of $z \simeq 2.3$ and $z \simeq 3.1$ based on the observability of $\text{Ly}\alpha$ given the wavelength range accessible to the medium resolution grating of PCWI. An effort was made to select targets evenly across this redshift range though operational constraints such as the number of required instrument settings on a single night or the times at which various targets were observable from Palomar at low airmass, limited this effort. An intentional effort was also made to select a wide range of absolute i-Band (rest-frame optical) magnitudes, in order to explore any dependence of the nebular emission on QSO brightness. The distributions of the pilot sample in redshift and absolute i-band magnitude is shown in Figure 2. A WISE color cut of $W2[4.8\mu\text{m}] - W3[11.6\mu\text{m}] > 4.8$, was used to identify heavily dust-obscured targets within the SDSS DR12Q which were expected to exhibit extended $\text{Ly}\alpha$ emission, as discussed in Bridge et al. (2013). The FLASHES pilot sample includes 9 of these dust-obscured targets, indicated in Figure 2 by the colorbar. We note that these 9 targets are not classical ‘Type II’ QSOs, as their spectra do contain broad line emission despite exhibiting heavily suppressed continuum emission. Over the course of the pilot survey, we included five additional targets from Trainor & Steidel (2012a, 2013) which were known to exhibit extended emission but lacked any IFS observations. In this work, a distinction is made between the total detection rate and the ‘blind’ detection rate, which excludes these five targets. Three targets were selected by searching the SIMBAD Astronomical Database based on coordinates and redshift to fill gaps in our observing schedule where no suitable targets were available from the SDSS

DR12Q. Finally, two soft constraints were applied in our selection. First, targets with few obscuring foreground stars and galaxies were preferred, as blended and nearby sources can make the data analysis step of isolating the nebular emission prohibitively complicated. Second, where radio data was available, radio-quiet sources were preferred. One of the goals of FLASHES is to study gas dynamics and cold inflows from the cosmic web, and the presence of jets associated with radio-loud quasars would complicate this analysis. Of the 48 pilot targets, only two are detected in radio and classify as radio loud ($f_{\nu}^{1.4\text{GHz}}/f_{\nu}^{4400\text{\AA}} \gtrsim 10$). Table 1 provides a breakdown of all of the pilot survey targets, coordinates and sources.

The FLASHES target selection is multi-pronged, and there are biases in the methodology towards radio-quiet quasars with fields relatively clear of nearby/foreground sources. Any biases in the SDSS DR12Q will also be inherited. As such, the authors caution that while this is the first large sample of its kind in this redshift range, the results of this work should not be quickly or trivially extrapolated to the wider galaxy population.

3. OBSERVATIONS AND ANCILLARY DATA

We observed 48 QSO fields between 2015 and 2018 on the 5-meter Hale telescope at Palomar using PCWI. PCWI is an image-slicer IFS mounted at the Cassegrain focus of the 5-meter Hale telescope at Palomar Observatory. The instrument field of view is $60'' \times 40''$ (approximately 480×320 pkpc² at $z \sim 2 - 3$). The longer axis is composed of 24 slices with a width of $\sim 2.5''$ and an in-slice pixel size of $\sim 0.55''$. Gratings and filters are interchangeable on PCWI. Our pilot observations used the medium resolution Richardson grating, which has a resolution of $R \simeq 2500$ and operates over a bandpass of 400 – 600 nm. With a spectral plate scale of 0.55 Å/px, the minimum resolution element $\Delta\lambda \sim 2\text{\AA}$ is sampled above the Nyquist rate. For all observations, we use a filter with a bandpass of 350 – 580 nm. For 44/48 of the targets, Nod-and-Shuffle (N&S) mode of PCWI was used (see Matuszewski et al. (2010) for details). In short, N&S allows for highly accurate sky subtraction, almost entirely free of systematic residuals, at the cost of bandwidth and statistical noise. The standard pilot observation consists of three 40 minute N&S observations (20 minutes on sky, 20 minutes on source), stacked for a total of 1 hour on source and 1 hour on sky. Seeing conditions at Palomar are generally such that the full-width at half-maximum (FWHM) of a point source is 1 – 2''. To increase the spatial sampling, the second and third N&S observations are dithered by $\pm 1''$ perpendicular to the direction of the slices. N&S mode was not used

for four targets in this sample (see Table 1). This was done on one observing run in the interest of spending more telescope time on source rather than on sky, but the increase in systematic sky residuals was not deemed worth it for future observations. For these, an A-B-B-A pattern was used to alternate between 20-minute science frames and 10-minute sky frames. Lastly, one target (HS1700+6416) has a significantly longer total exposure time, as it was one of the earliest targets to be observed. However, as it still represents an initial exploration, it is included in the Pilot sample.

The goal for each target was 60 minutes on source and 60 minutes on sky. For four targets we obtained 56, 54, 48 and 40 minutes in total due to time lost to poor weather. Multi-wavelength ancillary data were obtained for each target when available. Near- and far-UV data were obtained from GALEX (Bianchi et al. (2011)). Photometric u, g, r, i and z-band magnitudes were obtained from the Sloan Digital Sky Survey’s Photometric Catalog’s 12th data release (SDSS DR12 - Alam & et al. (2015)). 2MASS J, H and K-band magnitudes as well as WISE 3.35 μ m, 4.6 μ m, 11.6 μ m, and 22.1 μ m magnitudes were obtained from the AllWISE Data Release (Cutri & et al. 2013). Finally, 1.4GHz radio fluxes were obtained from the FIRST Survey (Helfand et al. 2015). All magnitudes and fluxes were converted to AB magnitudes for consistency. These data are presented in Appendix A.

4. DATA REDUCTION

4.1. Standard Pipeline Reduction

Initial data reduction is performed using the standard PCWI Data Reduction Pipeline¹, which converts raw, 2D science frames into flux-calibrated, three-dimensional cubes with real-world coordinate systems in RA, DEC and wavelength. A detailed description of PCWI calibration products, with useful reference images, is available in Matuszewski et al. (2010).

All frames are initially cosmic-ray subtracted, and bias subtracted. As PCWI is a Cassegrain-mounted instrument, there are sometimes slight offsets in the data due to gravitational flexure. These are corrected using a 2D cross-correlation method before the construction of 3D data products. The pipeline then maps from the 2D space of raw images to the 3D image coordinates (x, y, z) and on-sky/wavelength coordinates (α, δ, λ) using a ‘continuum bars’ image and an ‘arc-flat’ image, which have known spatial and spectral features, respec-

tively. The uneven illumination of the image slicer is then corrected for in two steps - first correcting the profile within each slice, and then correcting the slice-to-slice variation. Finally, a spectrophotometric standard star observation is used to convert detector counts to physical flux units. The final product of this pipeline is a three-dimensional, flux calibrated data cube for each individual exposure. For the four targets observed without N&S mode, sky subtraction was performed by extracting 2D sky spectra from the adjacent sky frames and scaling them on a slice-by-slice basis.

4.2. Cube Correction and Coadding

The large volume of data in this survey and complex nature of the 3D IFS data required the development of a toolkit for common reduction and analysis functions. `CWITools`² is a `Python3` toolkit written specifically for the analysis of PCWI and KCWI data. It is available publicly on Github and will be presented in more detail in a future paper.

Before co-adding, individual exposure cubes are first corrected by adjusting their world-coordinate system and trimming them. The RA/DEC coordinate system is corrected for each frame using the known location of a visible source in the field (typically the target QSO, though occasionally an adjacent star). The actual position of the source is measured in image coordinates, and then the coordinate system is updated such that that location accurately points to the known RA/DEC. This does not correct for any errors in rotation, though these are expected to be negligible. In a similar way, the wavelength axis is corrected using the positions of known sky emission lines. Finally, the cube is trimmed to only the wavelength range that which is shared by all slices, and edge pixels are trimmed off the spatial axes. The corrected and cropped input cubes are then coadded. `CWITools` uses a custom-built method for this in which each pixel in an input frame is mapped through two coordinate transformations: from input frame to sky and from sky to output frame. The input pixel is then represented by a polygon in output image coordinates, and the flux divided up appropriately onto the underlying pixel grid. This method allows for the input of frames with arbitrary spatial or spectral resolution and position-angle, and the coadding of variance frames with accurate error propagation.

5. DATA ANALYSIS

¹ PCWI DRP: <https://github.com/scizen9/pdrp>

² CWITools: <https://github.com/dbosul/CWITools>

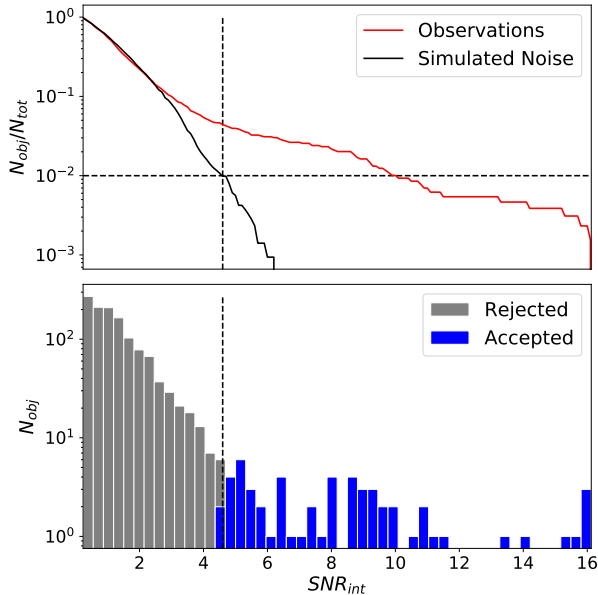


Figure 3. Top panel: Fraction of $> 1\sigma$ segmentation objects at or above a given SNR for simulated, smoothed noise (black line) and for the segmented objects in the FLASHES pilot sample (red line). The horizontal dashed line indicates a 1% occurrence rate, and the vertical dashed line represents the cut-off used to reject false positives. Bottom panel: a histogram of the integrated SNR values of 2D objects measured within a 300×300 pkpc² box of the target QSOs. The vertical line indicates the same cut-off used to select objects. The y-axis is displayed in log-scale for both plots.

In this section we describe the steps taken to extract extended Ly α emission in the CGM and produce scientific products from the data. We initially search for extended emission using a two-dimensional channel map method, which trades spectral resolution for an increased signal-to-noise ratio (SNR). Once emission is identified, we then analyze it in three dimensions to obtain kinematics and spectra.

5.1. Extraction of Nebular Emission in 2D

In order to identify extended emission, an initial exploration of the cubes is performed by making channel maps; series of pseudo-Narrow-Band (pNB) images in which the bandwidth is fixed and the central wavelength is stepped through some range of values. For the first iteration of these channel maps, we take the initial central wavelength to be the at the peak of Ly α emission in the quasar spectrum. We then use a velocity-width of $\delta v = 1000$ km s⁻¹ and step the central wavelength through a large range of ± 10000 km s⁻¹ in steps of 1000 km s⁻¹. White-light (WL) subtraction is performed in each channel to isolate nebular emission. A

WL image is formed by summing a wavelength layers on either side of the current channel. A width of 4000 km s⁻¹ ($\sim 60\text{\AA}$) is used for these adjacent regions. Pixels within a circular region of radius $\sim 1.5''$ around the QSO are then used to calculate a set of scaling factors between the images. The scaling factors are sigma-clipped at 3σ and the resulting mean is taken as the global scaling factor for the WL image. The WL image is then scaled and subtracted from the channel map. Data within the fitting radius cannot be used for measurement of extended emission.

Once emission is identified in a channel, a second channel map is generated with the same bandwidth, a narrower velocity range (± 2000 km s⁻¹) and smaller velocity step-size (200 km s⁻¹). This channel map is used to identify the best center for the pNB image. Finally, the new wavelength center is fixed and the bandwidth is varied from $\delta v = 200$ km s⁻¹ to $\delta v = 2000$ km s⁻¹ in steps of 200 km s⁻¹. The best bandwidth is then determined by selecting from this final set of pNB images based on visual inspection. For targets in which there was no obvious emission, the pNB was centered on the peak of Ly α emission in the QSO spectrum with a width of $\Delta v = 1000$ km s⁻¹. Continuum sources are identified and masked in each field using the 12th SDSS Data Release (Alam & et al. 2015) from the built in analysis tools of SAO-DS9 (Gastaud et al. 2002).

To create masks delineating emission in the pNB images, the images are first segmented into contiguous two-dimensional objects by the application of a low, positive signal-to-noise threshold. For our default maps we use an initial low threshold of 1σ , though we also produce masks using an initial threshold of 2σ to study the effects of this choice on our results. After the initial segmentation, the integrated signal-to-noise ratio (SNR_{int}) of each object is calculated, and a high threshold is applied to reject false positives. The resulting regions are converted into a binary mask delineating the detected emission, which we denote $M(x, y)$. To determine the appropriate integrated SNR threshold, we run the segmentation and thresholding process on simulated data containing only Gaussian noise which has been smoothed with the same kernel as the real data. We then select a cutoff in the distribution of integrated SNR values that returns a simulated false positive rate of $< 1\%$. This choice places the upper limit of the expected number of false positives in the sample below one (in the scenario where all detected objects have the minimum SNR_{int}) This exercise yields a cutoff of SNR_{int} $> 4.5\sigma$. Figure 3 shows the distribu-

tions of integrated SNR values from both the simulated and real data, as well as the cutoff used.

5.2. Characterizing 2D Morphology

In order to highlight different characteristics, we measure the size of the nebulae in three ways. First, we use the maximum extent of the nebula from its flux-weighted centroid, R_{\max} . Secondly, we define an *effective* radius to be the radius of an equivalent circular area, i.e., $R_{\text{eff}} = \sqrt{\text{Area}/\pi}$. We emphasize that R_{eff} is not a true radius, but a characteristic scale. Finally, we measure the flux-weighted root-mean-square radius, $R_{\text{rms}} = \sqrt{\langle R^2 \rangle_f}$, using the flux values under the 2D nebular mask. While R_{\max} and R_{eff} give a sense of the maximum and average extent of the nebula, respectively, R_{rms} size gives a sense of the characteristic scale at which most of the emission is concentrated.

Beyond measurement of size, the 2D morphology is characterized by three parameters; eccentricity (i.e. asymmetry), displacement, and covering factor. To quantify the symmetry of the nebulae and allow for direct comparison with existing literature, we adopt the same measurement of spatial symmetry as presented in A18. This parameter, α , is derived from the second-order spatial moments and reflects the ratio of the semi-minor axis (b) to the semi-major axis (a) of the emission (i.e., $\alpha = b/a$). We then convert it to an elliptical eccentricity parameter (e), which we find to be more intuitive, following:

$$e = \sqrt{1 - b^2/a^2} = \sqrt{1 - \alpha^2} \quad (1)$$

The displacement, which we denote d_{QSO} , is the projected physical distance (in proper kiloparsecs) between the flux-weighted centroid of the nebular emission and the quasar.

5.3. Radial Profiles

Radial surface brightness profiles are measured from a minimum projected radius of 15 pkpc to a maximum radius of 150 pkpc in logarithmic bins of 0.1 dex. All of the detected emission in this sample falls within this range. The average surface-brightness and variance within each annular region are measured and a survey-wide average radial profile is calculated using the integrated signal-to-noise of the emission in each nebula as weights. The 2D object mask is not applied when calculating the circularly averaged surface-brightness profile, but the locations of known and subtracted continuum sources are masked. The covering factor is calculated using the same radial bins, and defined as the fraction of pixels in each annular region above an SNR of 2σ .

5.4. Luminosities

The integrated luminosity of each nebula is calculated following

$$L_{\text{tot}} = \frac{(\delta\theta)^2}{4\pi D_L^2(z)} \sum_x \sum_y \text{SB}(x, y) M(x, y) \quad (2)$$

where $\text{SB}(x, y)$ is the 2D surface-brightness map in units of $\text{erg s}^{-1} \text{cm}^{-2} \text{arcsec}^{-2}$, $M(x, y)$ is the binary 2D mask defined earlier, $\delta\theta$ is the angular size of a pixel, and $D_L(z)$ is the luminosity distance at the redshift of the target. We note that integrated luminosities are sensitive to the surface-brightness threshold used to define $M(x, y)$, any comparison to luminosities reported in other works should consider the differences in cosmic dimming-adjusted surface brightness limits.

5.5. Point-source Subtraction in 3D

CWITools performs 3D point-spread function (PSF) subtraction in a similar fashion to Borisova et al. (2016), which is a basic extrapolation of the pNB method, described earlier, to 3D. A white-light image is formed by summing all of the wavelength layers of the cube, which is then used to identify the positions of any point sources. For each point source above a certain signal-to-noise threshold, the following routine is repeated: For each wavelength layer in the cube, a broad-band (i.e., white-light) image centered on the current wavelength layer is formed by summing over a large spectral range ($\sim 100\text{\AA}$). This image is then scaled and subtracted from the wavelength layer using the method described in Section 5.1. The underlying assumption of this technique is that the shape of the PSF will be dominated by white-light, not nebular emission. In the case of obscured quasars with faint continuum or quasars with particularly bright extended emission, the wavelength range containing nebular emission may be masked to prevent it being used for the white-light image. A small inner radius roughly equal to the seeing ($\sim 1''$) is used to calculate the scaling factors, and the scaled WL image is subtracted out to a larger radius, typically a few times the seeing ($\sim 5''$). Once this PSF subtraction is completed for all detectable point sources, any remaining continuum or scattered light is subtracted (if necessary) using a low-order ($k = 1$ or 2) polynomial fit to the spectrum in each spaxel. If strong nebular emission is identified, it can be masked during this fitting process to avoid over-fitting. Finally, the PSF cores of bright sources that have been subtracted are masked to prevent noisy residuals influencing any measurements later on. As with the 2D pNB images, the positions of known continuum sources are identified and masked using sources from the 12th SDSS Data Release (Alam

& et al. 2015).

5.6. Integrated Nebular Spectra and Line-Fitting

To create an approximate 3D mask encompassing the emission, the spatial object mask, $M(x, y)$ is extended along the wavelength axis over the same range as was used to form the final pNB image. Nebular spectra are obtained by summing over the spatial axes under the 3D mask. The spectra are fit with both a simple Gaussian model, a model consisting of multiple (1 – 4) Gaussian components, and a simple linear model. To determine which model best represents the data, we calculate the Bayesian Information Criterion (BIC) for each, following

$$\text{BIC} = n \ln(RSS/n) + k \ln n \quad (3)$$

where n is the number of independent variables (i.e., length of the spectrum), k is the number of free parameters in the model, and RSS is the residual sum of squares of the model. Lower BIC values indicate a better representation of the data. Weights representing the relative likelihood of a set of models can be derived from the BIC values as:

$$w_i = \frac{\exp(-\frac{1}{2}\Delta_i(\text{BIC}))}{\sum_j \exp(-\frac{1}{2}\Delta_j(\text{BIC}))} \quad (4)$$

where $\Delta_i(\text{BIC})$ is the difference between the i th BIC value and the minimum BIC value of the set (Wagmakers & Farrell 2004). The value $0 \leq w_i \leq 1$ corresponds to the relative likelihood that the i th model is the best representation of the data (among those considered). The linear model is included as a simpler alternative in order to validate the single-component Gaussian models; if only Gaussian models were considered, the BIC would still indicate a single-component Gaussian as the best fit for pure noise. This multiple-component fit provides an important piece of contextual information when interpreting the global dispersions of the nebulae - as complex line shapes with multiple components can appear quite broad when viewed as a single Gaussian, or otherwise treated as a single kinematic component (e.g., by calculating the second moment).

To create a stacked Ly α spectrum from the 42 individual detections, spectra are linearly interpolated onto a rest-frame wavelength grid ranging from 1200 Å to 1230 Å with a sampling rate of 0.14 Å/px (approximately the PCWI sampling around Ly α at $z = 3$). As there is more than one measure of redshift (e.g. the flux-weighted center of emission vs. the systemic QSO redshift), we create four versions of the stacked spectrum, each using a different central wavelength (i.e., redshift) to convert to

rest-frame units: (i) the systemic QSO redshift given in DR12Q, (ii) the flux-weighted center of Ly α emission, (iii) the peak of Ly α emission in the QSO spectrum, and (iv) the HeII $\lambda 1640$ redshift from DR12Q.

5.7. 2D Moment Maps

Two-dimensional first and second flux-weighted z -moment maps are calculated as:

$$\mu_{\lambda,1} = \frac{\sum_k \lambda(k) I_k}{\sum_k I_k} \quad (5)$$

$$\mu_{\lambda,2} = \sqrt{\frac{\sum_k (\lambda_k - \mu_1)^2 I_k}{\sum_k I_k}} \quad (6)$$

where I_k is the k^{th} wavelength layer of the intensity cube and λ_k is the wavelength at that layer. I and μ are both two-dimensional arrays with the spatial indices (i, j) omitted for simplicity (i.e., $I_k = I_{ijk}$). Prior to calculating the moments, the data is smoothed by a $1 \times 1 \times 1$ (FWHM) Gaussian kernel, which corresponds to 2D Gaussian with a FWHM $\simeq 0.6''$ and by a 1D Gaussian with a FWHM of 0.55\AA .

As a statistical moment is not well defined for a distribution with negative weights, some non-negative threshold must be applied to the spectra before calculating the first or second moment. For bright signals, a high SNR threshold can be applied which rejects virtually all noise while also retaining enough signal for an accurate measurement. However, for fainter signals, it can be challenging to find a threshold which satisfies both of these requirements. A simple positive threshold (i.e., $F_\lambda > 0$) can be applied, positive fluctuations in the background noise will then bias the calculation. For the calculation of the first moment, μ_1 , an iterative approach can be used to overcome this. The effect of evenly distributed noise (in a well background-subtracted signal) will be to bias the result towards the center of whichever wavelength window is used. If the wavelength window is centered on the true first moment, then this biasing effect will be negligible. As such, if we perform this calculation iteratively, updating the center of the window each time to the new value of μ_1 , the window center will eventually converge on the true value. If the size of the wavelength window used for the calculation is also reduced as the solution converges, this further mitigates any biasing effect from unevenly distributed noise. We use this method to determine the first moment (i.e. velocity center) of the spectra in each spaxel, with a starting window size of 25\AA (to fully explore the range used for the pNB images), reduced in steps of $\Delta\lambda = 1\text{\AA}$ until a minimum window size of

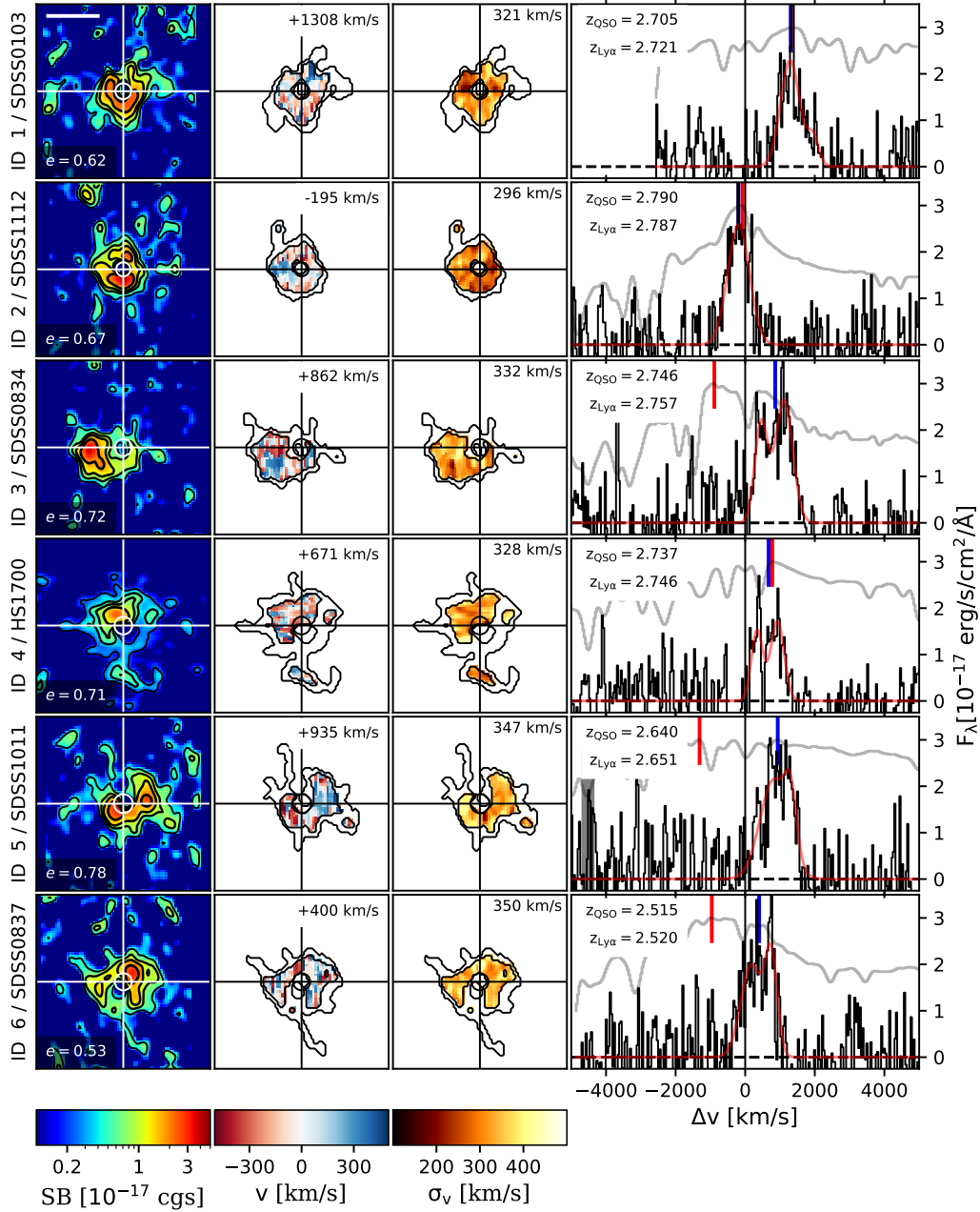


Figure 4. FLASHES Pilot survey observations (ID 1-6). The leftmost three columns show Ly α surface brightness, velocity, and dispersion in 350×350 pkpc² tiles around the QSOs. Surface brightness is in $\text{erg s}^{-1} \text{cm}^{-2} \text{arcsec}^{-2}$ with a log-scale colorbar. The white bar in the top pNB image shows 100 pkpc. The eccentricity of the emission under the 1σ object mask is shown in the lower left corner of each pNB image. Continuum sources in each field have been subtracted and masked. Velocity data is only shown for $\text{SNR} > 2\sigma$ spaxels, while the full mask outline is shown in black. The rightmost column shows integrated nebular spectra (black) and scaled QSO spectra (grey). The spectra are summed over the full 1σ object masks and shown in units of $10^{-17} \text{erg s}^{-1} \text{cm}^{-2} \text{\AA}^{-1}$. Spectra are shown in velocity space and centered on the QSO redshift. Red lines indicate the peak of the QSO emission within $\pm 5000 \text{ km s}^{-1}$ of Ly α and blue lines indicate the flux-weighted centers of nebular emission. A very bright mercury sky emission line (*Hg* $\lambda 4358.3$) is masked in some spectra and shown here as a vertical black band wherever it appears.

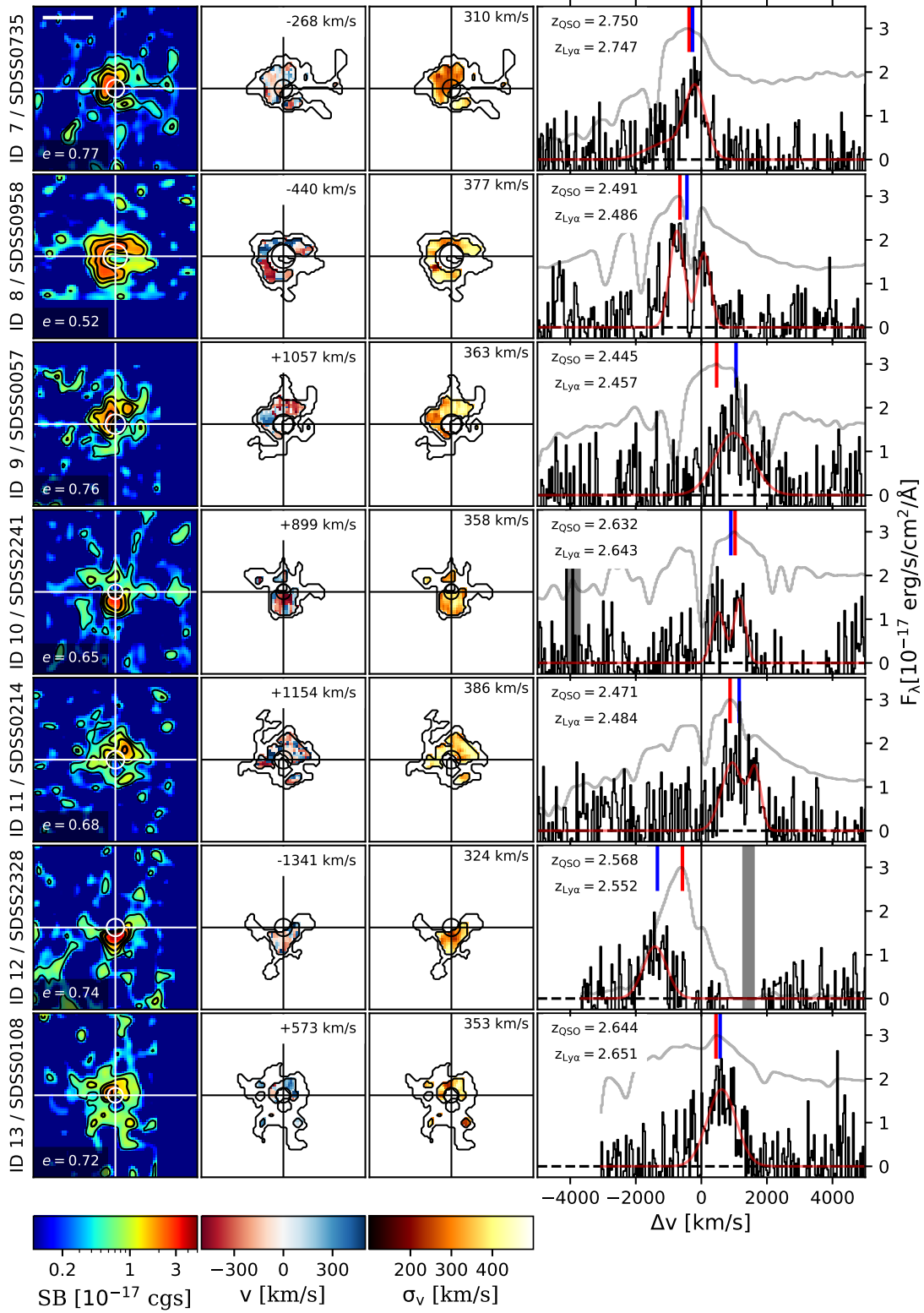


Figure 4. (continued) FLASHES Pilot survey observations (ID 7-13).

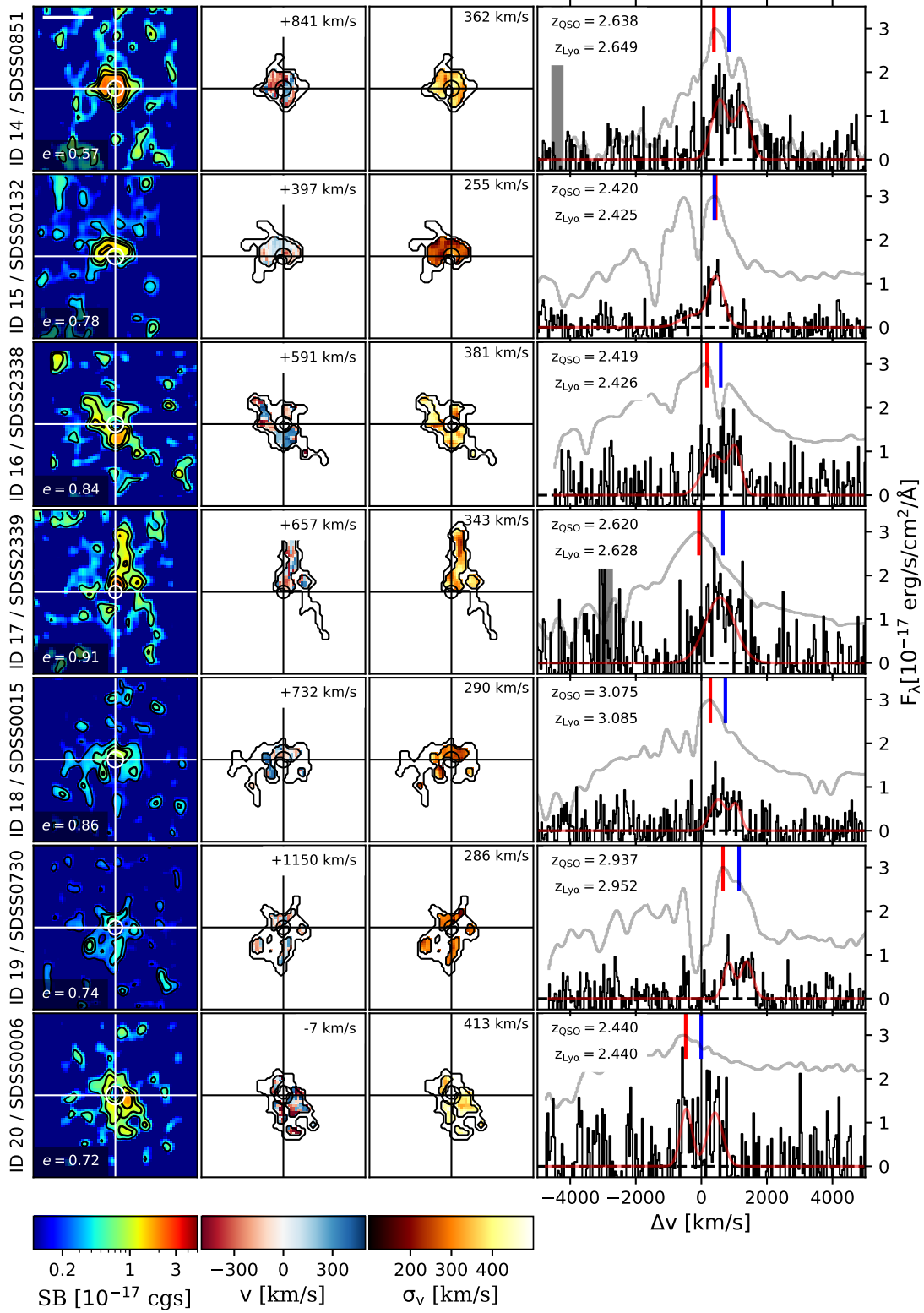


Figure 4. (continued) FLASHES Pilot survey observations (ID 14-20).

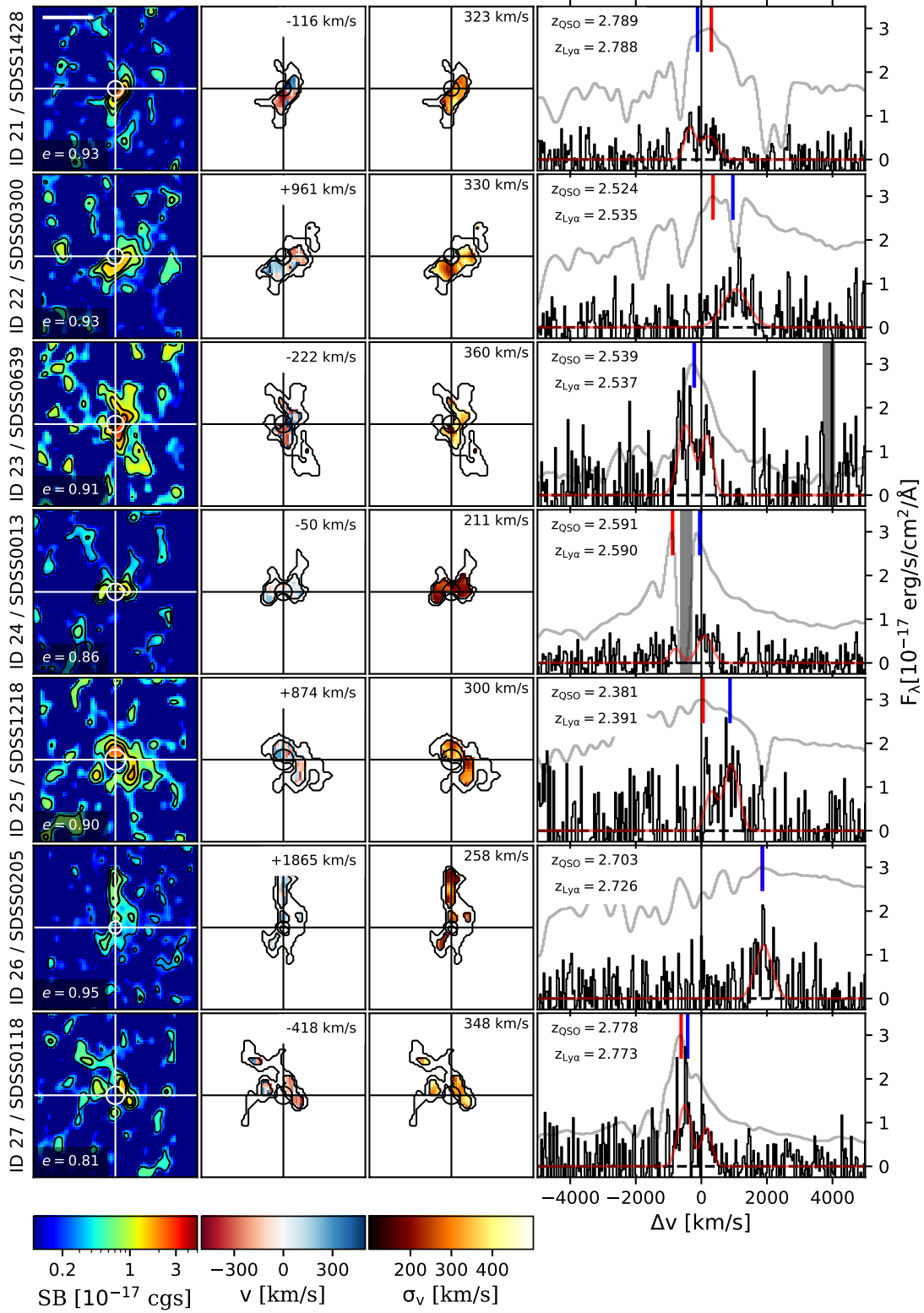


Figure 4. (continued) FLASHES Pilot survey observations (ID 21-27).

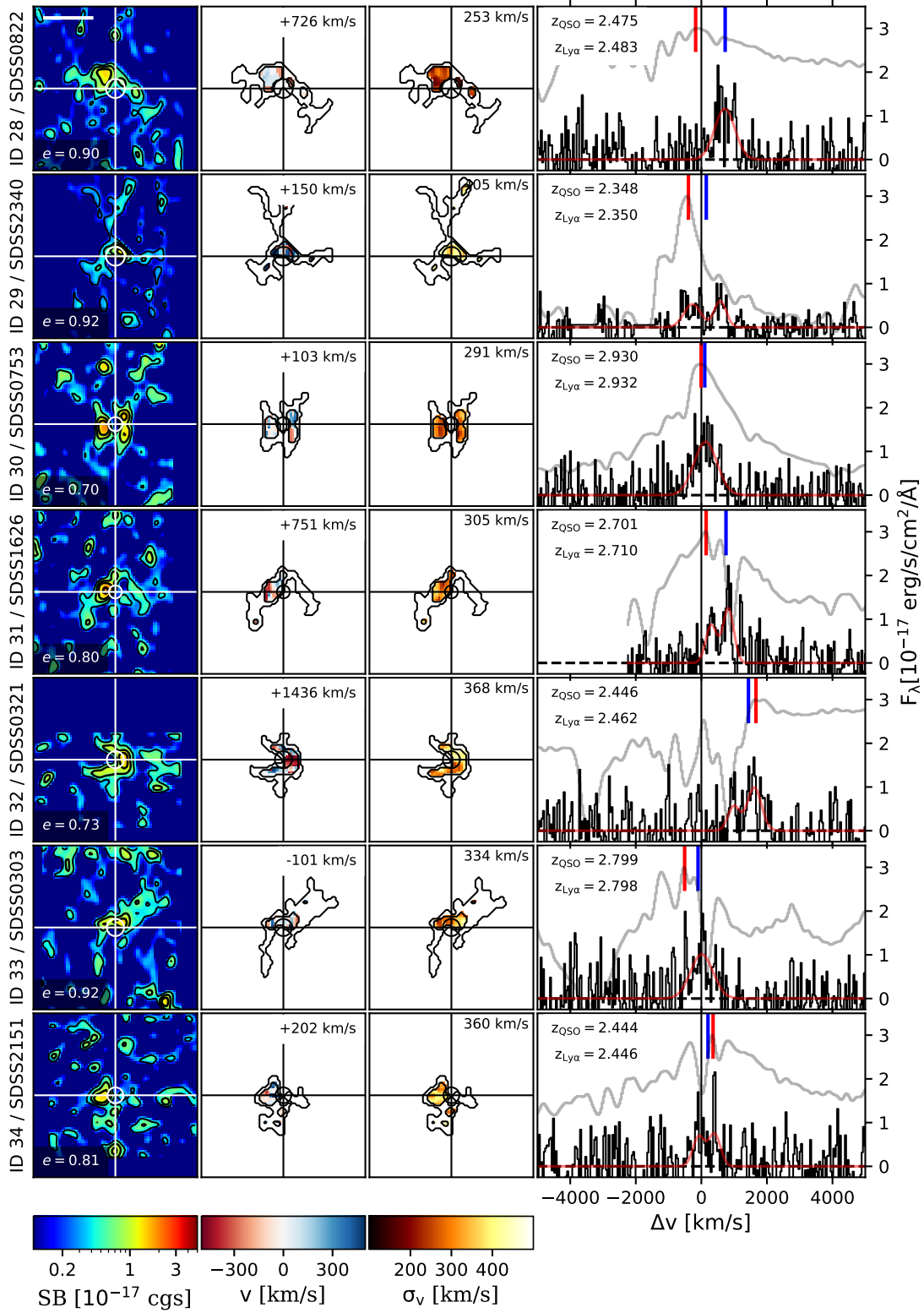


Figure 4. (continued) FLASHES Pilot survey observations (ID 28-34).

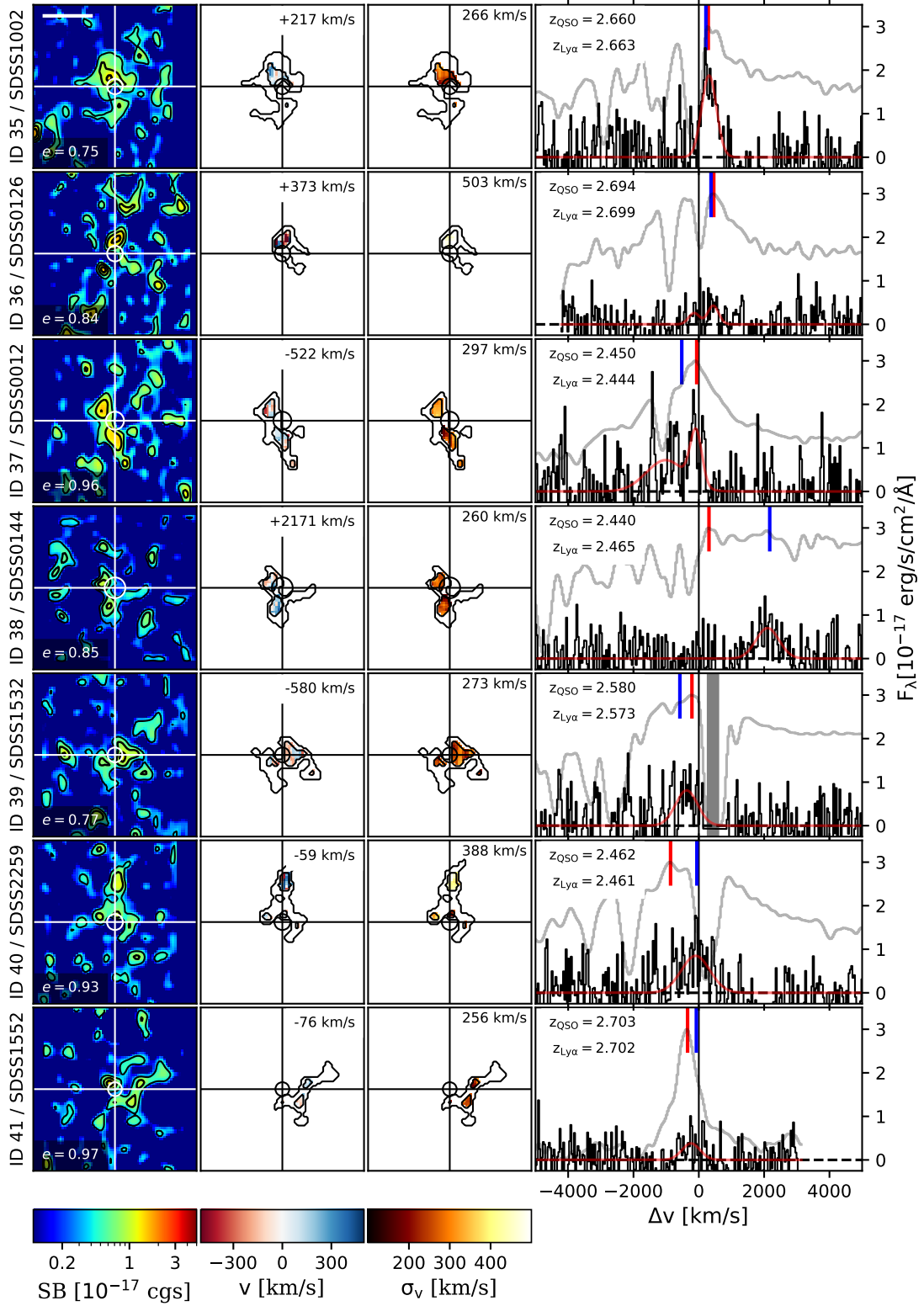


Figure 4. (continued) FLASHES Pilot survey observations (ID 35-41).

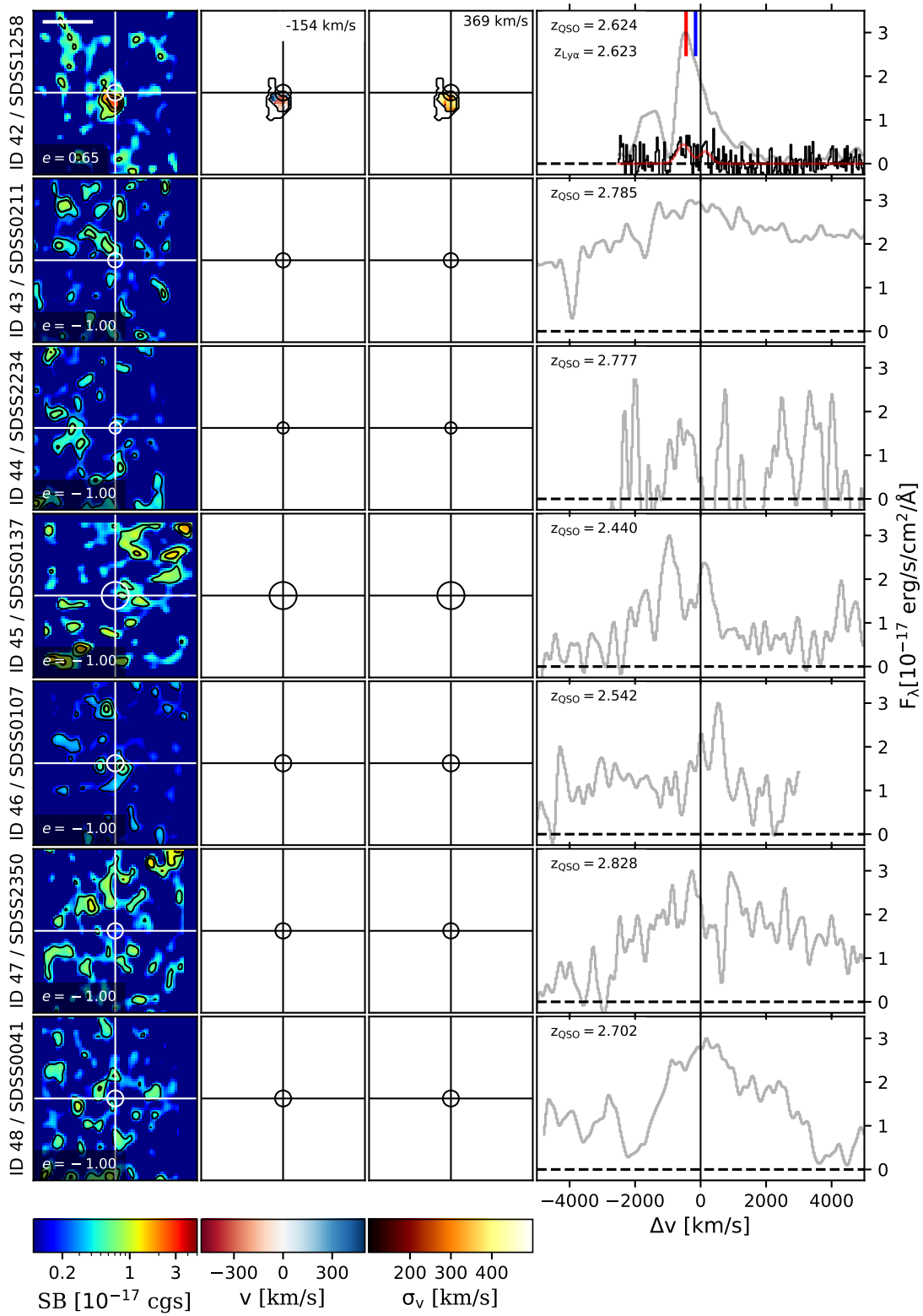


Figure 4. (continued) FLASHES Pilot survey observations (ID 42-48).

10\AA is reached. Appendix B provides an illustration of this method.

For the second moment, a convergent method cannot be used to the same effect, as the influence of normally distributed noise on the second moment is to unilaterally increase its value. Instead, we apply a basic non-negative threshold and treat the derived values as upper limits. The spatially resolved maps still provide our only insights into the 2D distribution of the second moment, and as such are valuable despite this limitation. We can rely on line-fitting of the integrated nebular spectrum (see Section 5.6) for more robust measurements of the global dispersions of the nebulae.

Once the moments are calculated, Ly α velocity and dispersion maps can be derived as:

$$v(i, j) = \left(\frac{\mu_{\lambda,1}(i, j) - \lambda_0}{\lambda_0} \right) c \quad (7)$$

$$\sigma_v(i, j) = \left(\frac{\mu_{\lambda,2}(i, j)}{\lambda_0} \right) c \quad (8)$$

where λ_0 is the flux-weighted average wavelength of the integrated nebular spectrum, $\mu_{\lambda,1}(i, j)$ is the first

moment in wavelength (Eq. 5) at that position, and c is the speed of light in vacuum. For each nebula, we also calculate the flux-weighted, one dimensional root-mean-square velocity along the line of sight, $v_{\text{rms}} = \sqrt{\langle v^2 \rangle}_f$. To be clear, this is the root-mean-square of velocities in individual spaxels *relative* to the flux-weighted average velocity of the nebula. Finally, we measure the offset between the the flux-weighted average velocity of the nebula and three key wavelengths; the wavelength of Ly α at the systemic redshift of the QSO ($\lambda_{\alpha, \text{QSO}}$), the wavelength of the peak of Ly α emission in the QSO spectrum ($\lambda_{\alpha, \text{peak}}$) and the wavelength of Ly α at the HeII $\lambda 1640$ redshift of the QSO ($\lambda_{\alpha, \text{HeII}}$).

$$\Delta v_{\text{QSO}} = \left(\frac{\lambda_{\alpha, \text{QSO}} - \lambda_0}{\lambda_0} \right) c \quad (9)$$

$$\Delta v_{\text{peak}} = \left(\frac{\lambda_{\alpha, \text{peak}} - \lambda_0}{\lambda_0} \right) c \quad (10)$$

$$\Delta v_{\text{HeII}} = \left(\frac{\lambda_{\alpha, \text{HeII}} - \lambda_0}{\lambda_0} \right) c \quad (11)$$

Table 2. Measured CGM properties from the FLASHES Pilot Survey.

ID	Target Name	L_{43}^a erg s $^{-1}$	R_{eff} pkpc	R_{rms} pkpc	R_{max} pkpc	d_{QSO} pkpc	e (0-1)	z_{QSO}	$z_{\text{Ly}\alpha}$	Δv_{QSO} km s $^{-1}$	Δv_{peak} km s $^{-1}$	σ_v km s $^{-1}$	N_G (0-4)
1	SDSS0103+1316	14.1	70.8	47.7	104.0	6.9	0.62	2.705	2.721	+1308	-46	327	2
2	SDSS1112+1521	13.3	61.1	41.5	102.6	8.5	0.67	2.790	2.787	-195	-189	310	1
3	SDSS0834+1238	14.0	68.7	47.3	126.9	43.6	0.72	2.746	2.757	+862	+1493	458	3
4	HS1700+6416	9.9	82.7	62.8	146.7	8.3	0.71	2.737	2.746	+671	-140	373	2
5	SDSS1011+2941	13.9	73.5	53.0	133.4	19.3	0.78	2.640	2.651	+935	+2243	432	4
6	SDSS0837+1459	11.8	73.9	54.0	147.9	5.7	0.53	2.515	2.520	+400	+665	418	2
7	SDSS0735+3744	10.1	65.5	53.0	138.0	14.0	0.77	2.750	2.747	-268	+105	383	2
8	SDSS0958+4703	13.7	66.4	46.1	90.5	4.9	0.52	2.491	2.486	-440	+370	689	3
9	SDSS0057+0346	8.0	61.8	45.3	97.4	14.8	0.76	2.445	2.457	+1057	+631	561	1
10	SDSS2241+1225	7.3	55.9	41.3	93.2	1.1	0.65	2.632	2.643	+899	-51	406	2
11	SDSS0214+1912	7.1	64.2	47.0	103.0	14.2	0.68	2.471	2.484	+1154	+204	508	2
12	SDSS2328+0443	6.8	47.9	37.8	90.4	19.1	0.74	2.568	2.552	-1341	-646	349	1
13	SDSS0108+1635	10.6	67.2	53.1	111.4	11.5	0.72	2.644	2.651	+573	-57	405	1
14	SDSS0851+3148	7.8	47.6	31.5	68.0	7.2	0.57	2.638	2.649	+841	+497	513	2
15	SDSS0132+3326	3.5	49.9	34.7	76.5	19.4	0.78	2.420	2.425	+397	+871	307	2
16	SDSS2338+1504	5.9	57.6	48.0	124.7	2.1	0.84	2.419	2.426	+591	+540	479	2

Table 2 *continued*

Table 2 (continued)

ID	Target Name	L_{43}^a	R_{eff}	R_{rms}	R_{max}	d_{QSO}	e	z_{QSO}	$z_{\text{Ly}\alpha}$	Δv_{QSO}	Δv_{peak}	σ_v	N_G
		erg s ⁻¹	pkpc	pkpc	pkpc	pkpc	(0-1)			km s ⁻¹	km s ⁻¹	km s ⁻¹	(0-4)
17	SDSS2339+1901	7.2	54.3	55.4	161.0	52.4	0.91	2.620	2.628	+657	+693	447	2
18	SDSS0015+2927	6.1	58.2	50.7	102.7	16.6	0.86	3.075	3.085	+732	+459	349	2
19	SDSS0730+4340	3.9	57.8	46.0	93.9	18.5	0.74	2.937	2.952	+1150	+527	346	2
20	SDSS0006+1614	5.6	56.2	43.8	81.0	24.5	0.72	2.440	2.440	-7	+667	516	2
21	SDSS1428+2336	4.3	41.4	33.3	74.7	11.9	0.93	2.789	2.788	-116	-420	366	2
22	SDSS0300+0222	4.8	51.1	41.6	95.9	14.4	0.93	2.524	2.535	+961	+453	389	1
23	SDSS0639+3819	9.1	57.8	55.9	115.3	21.2	0.91	2.539	2.537	-222	-10	380	3
24	SDSS0013+1630	2.8	42.4	33.4	81.7	15.2	0.86	2.591	2.590	-50	+336	230	3
25	SDSS1218+2414	5.7	54.5	42.9	86.0	23.5	0.90	2.381	2.391	+874	+822	377	3
26	SDSS0205+1902	4.0	54.1	54.7	107.7	33.9	0.95	2.703	2.726	+1865	+59	246	1
27	SDSS0118+1950	5.7	53.6	53.9	113.6	35.2	0.81	2.778	2.773	-418	+199	382	2
28	SDSS0822+1626	4.1	56.9	56.1	119.1	10.2	0.90	2.475	2.483	+726	+658	318	2
29	SDSS2340+2418	2.5	57.3	70.6	133.5	39.5	0.92	2.348	2.350	+150	+464	602	3
30	SDSS0753+4030	6.8	47.4	37.0	88.5	2.9	0.70	2.930	2.932	+103	+109	343	1
31	SDSS1626+4858	4.5	48.0	47.1	92.9	11.6	0.80	2.701	2.710	+751	+605	349	2
32	SDSS0321+4132	3.5	46.5	36.8	69.8	4.4	0.73	2.446	2.462	+1436	-494	342	2
33	SDSS0303+3838	5.5	55.0	56.4	134.0	27.6	0.92	2.799	2.798	-101	+445	342	1
34	SDSS2151+0921	2.6	44.4	36.6	69.9	21.0	0.81	2.444	2.446	+202	-154	305	2
35	SDSS1002+2008	5.4	53.4	45.3	94.2	10.4	0.75	2.660	2.663	+217	-72	229	1
36	SDSS0126+1559	2.5	34.0	29.6	65.2	22.3	0.84	2.694	2.699	+373	+870	442	2
37	SDSS0012+3344	4.0	45.1	44.7	91.9	15.0	0.96	2.450	2.444	-522	-498	600	3
38	SDSS0144+0838	1.9	41.6	38.7	77.9	14.8	0.85	2.440	2.465	+2171	+1626	321	1
39	SDSS1532+3059	3.3	48.2	40.8	78.7	17.5	0.77	2.580	2.573	-580	-330	319	1
40	SDSS2259+2326	3.0	46.5	46.8	95.8	41.7	0.93	2.462	2.461	-59	+766	452	1
41	SDSS1552+1757	2.7	38.5	45.3	81.7	50.5	0.97	2.703	2.702	-76	+266	280	1
42	SDSS1258+2123	3.5	30.9	21.1	52.3	17.6	0.65	2.624	2.623	-154	+289	292	2

NOTE—From left to right: target ID, target name, luminosity (L_{43}), sizes (R_{eff} , R_{rms} , R_{max}), displacement (d_{QSO}), eccentricity (e), systemic redshift (z_{QSO}), redshift of CGM Ly α emission ($z_{\text{Ly}\alpha}$), velocity offset from systemic redshift (Δv_{QSO}), velocity offset from peak of Ly α emission in the QSO spectrum (Δv_{peak}), dispersion as fit by a single Gaussian (σ_v), and best-fit number of Gaussian components (N_G).

$$^a L_{43} = L/10^{43} \text{ erg s}^{-1}$$

6. RESULTS

In this section we present the 2D morphologies, eccentricities, radial profiles, kinematic properties and integrated spectra of the nebulae detected in the FLASHES Pilot sample. For the survey as a whole we present an averaged radial profile, covering factors, and distributions of kinematics. In order to provide a more complete physical picture of each QSO environment, the basic observational data (surface brightness, velocity, dispersion and integrated spectra) are displayed side-by-side in the extended Figure 4 for each target.

6.1. Size and Luminosity

The leftmost column of Figure 4 shows the pNB images generated following Section 5.1. We detect nebulae (i.e. regions of emission with $\text{SNR}_{\text{int}} > 4.5$) around 42 of the 48 objects in our sample. Of these, 26 have effective diameters $D_{\text{eff}} = 2R_{\text{eff}} \geq 100$ pkpc; meeting the criterion for "giant" nebulae. Excluding the five targets obtained from literature, which were previously known to contain extended emission, we find a detection rate of 20/42 for giant Ly α nebulae and 37/42 for extended Ly α emission in general. The nebulae

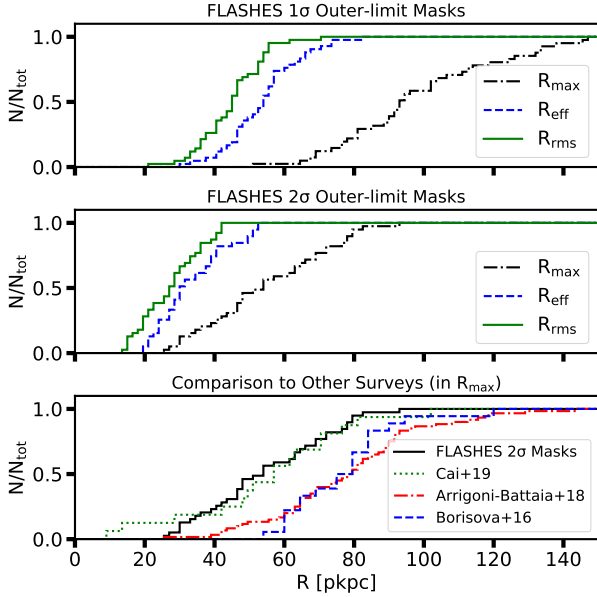


Figure 5. Cumulative distributions of the sizes of the detected nebulae. The top panel shows the three characteristic sizes as measured from the 1σ FLASHES object masks. The middle panel shows those measured from masks with a 2σ outer limit. The bottom panel compares the maximum extent of the FLASHES nebulae with those reported in A18, B16 and C19. We note that some of the sizes presented in C19 are lower limits, as the emission reached the edge of their field of view.

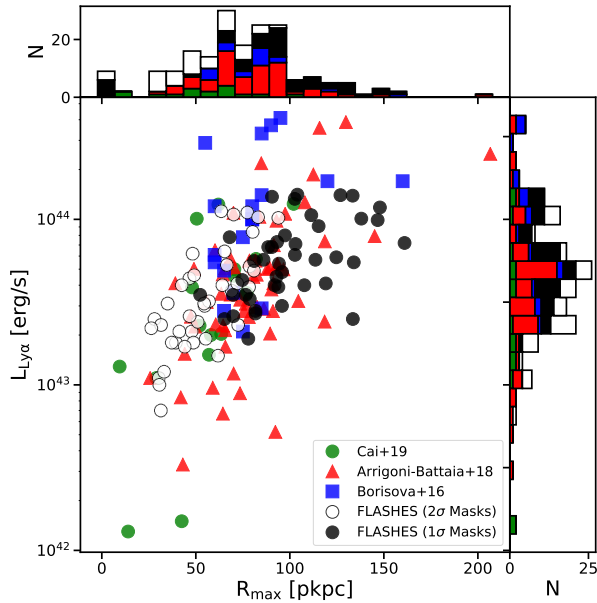


Figure 6. Luminosity and size (R_{\max}) comparison of FLASHES (1σ and 2σ object masks) with A18, B16 and C19. The distributions of R_{\max} and $L_{Ly\alpha}$ are shown as stacked histograms on the top and right, respectively.

Table 3. Distributions of Measured Sizes

	Min(R)	Max(R)	Mean(R)	Median(R)	σ (R)
	pkpc	pkpc	pkpc	pkpc	pkpc
R_{\max}	49	161	87	93	41
R_{eff}	31	83	47	53	21
R_{rms}	21	71	39	45	18

are found to have projected radii on the order of tens of proper kiloparsecs, with $R_{\text{eff}} \simeq 31 - 83$ pkpc and $R_{\text{rms}} \simeq 21 - 71$ pkpc. The maximum extent of the nebulae are found to be significantly larger than the effective radii ($R_{\max} \simeq 49 - 161$ pkpc) indicating some degree of asymmetry. We plot the cumulative distribution functions for each measurement of size for both the 1σ and 2σ outer-limit object masks in the top two panels of Figure 5. In the bottom panel, we compare our distribution of R_{\max} values (using 2σ masks) to those reported in C19, A18 and B16. Table 3 below summarizes the distributions of these three parameters. The integrated luminosities range from $L_{\min} = 1.9 \times 10^{43}$ erg s $^{-1}$ to $L_{\max} = 14.1 \times 10^{43}$ erg s $^{-1}$, with mean $L_{\text{avg}} = 6.4 \times 10^{43}$ erg s $^{-1}$ and standard deviation $\sigma_L = \pm 3.6 \times 10^{43}$ erg s $^{-1}$. These are in broad agreement with the values reported in A18, but slightly fainter than those reported in B16. Figure 6 shows the nebulae in the parameter space of luminosity and size, again for both object masks ($1 - 2\sigma$ segmentation thresholds).

6.2. 2D Morphology

From a quick glance at the pNB images in Figure 4, it is clear that there is quite a spread in the spatial symmetry of the nebulae. As discussed earlier, we quantify this using the elliptical eccentricity parameter, $0 < e \leq 1$, where $e = 0$ indicates a perfectly circular morphology. The calculated values are displayed in the lower-left corner of the pNB images, as well as in Table 2. The detected nebulae are found to exhibit highly eccentric morphologies, with a minimum of 0.52, a maximum of 0.97, and a mean (median) of 0.79 (0.78) and a standard deviation $\sigma_e = 0.12$. A few highly eccentric targets (e.g., IDs 17, 23, 26) appear to have narrow filamentary emission on one or both sides of the QSO. The majority of detections are centered approximately on the quasar itself, with displacements $d_{QSO} \lesssim 20$ pkpc. However, a small number of targets have emission which is more significantly displaced from the QSO, with the highest displacement being 52 pkpc.

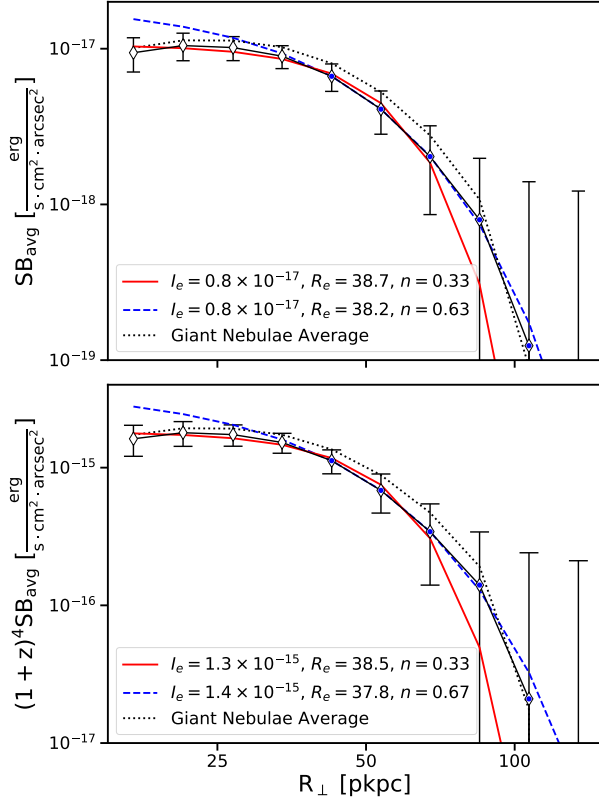


Figure 7. Circularly averaged radial profiles of the detected CGM, centered on the QSOs. The profiles are displayed in log-log space, and the radial bins are defined with logarithmic sizes of 0.1 dex. Solid black lines with diamond markers indicates the survey-wide averages, while the dotted black lines indicate the average of the giant nebulae only. The top panel shows the averaged profiles in observed surface brightness, while the bottom panel shows the average of the profiles after scaling each by $(1+z)^4$ to correct for cosmological surface brightness dimming. Solid red lines indicate Sérsic fits to the data, with the fit parameters shown in the figure legend.

6.2.1. Radial Profiles

Figure 7 shows the average radial surface-brightness profiles of the FLASHES Pilot survey detections. The sample-wide average is shown alongside the average for giant nebulae. The profiles are shown both in observed surface brightness (top panel) and with the surface brightness scaled by $(1+z)^4$ to account for cosmic dimming (bottom panel). The sample-wide average profile peaks in observed surface brightness at around $SB_{\max}^{\text{obs}} \simeq 1 \times 10^{-17} \text{ erg s}^{-1} \text{ cm}^{-2} \text{ arcsec}^{-2}$ ($SB_{\max}^{(1+z)^4} \simeq 2 \times 10^{-15} \text{ erg s}^{-1} \text{ cm}^{-2} \text{ arcsec}^{-2}$). The giant nebulae are marginally brighter on average over the full radial extent of the profiles. The bulk of emission appears to fall within 50 pkpc of the quasar, with the circularly averaged surface brightness falling by almost an or-

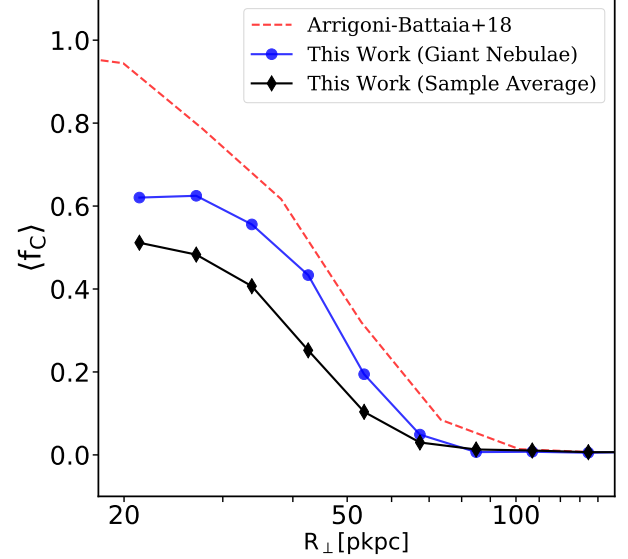


Figure 8. Covering fraction of values greater than 2σ as a function of radius. The average of all detections is shown with black diamond markers, the average profile of giant nebulae is shown with blue circular markers, and an approximation of the equivalent profile reported in A18 is shown as a dashed red line. Values are plotted as lower limits to indicate the sensitivity-dependence of this result.

der of magnitude at this distance. The averaged profiles appear to have a core that extends out approximately 30 – 40 pkpc. We fit the survey-wide averaged radial profiles with a Sérsic profile (Sérsic 1963) and display the best-fit parameters in the legend of Figure 7. The emission appears to be well described out to $R \simeq 100$ pkpc by a profile with Sérsic index $n \simeq 0.3$, half-light radius $R_e \simeq 38$ pkpc, and intensity (surface brightness) at the half-light radius $I_e = 8 \times 10^{-18} \text{ erg s}^{-1} \text{ cm}^{-2} \text{ arcsec}^{-2}$ ($I_e^{(1+z)^4} = 1.3 \times 10^{-15} \text{ erg s}^{-1} \text{ cm}^{-2} \text{ arcsec}^{-2}$). We note that an exponential profile is a Sérsic with $n = 1$, and that a parameter space of $n = 0.1 - 6.0$ was explored during the fitting process using a stochastic optimizer (differential evolution from SciPy - (Virtanen et al. 2019; Storn & Price 1997)) which is less susceptible to local minima than standard gradient descent algorithms. To test whether this fit is sensitive to the inner radii (i.e., sensitive to residuals of PSF subtraction), we also fit a profile using only the data at radii larger than 40 pkpc. This fit is also shown in Figure 7. The half-light radii and intensity remain within $\pm 10\%$ of the previous values, and the Sérsic index increases to $n = 0.64 - 0.68$, which is closer to an exponential profile but still notably different.

Figure 8 shows the covering factor as a function of projected radius for three profiles; the sample-wide average,

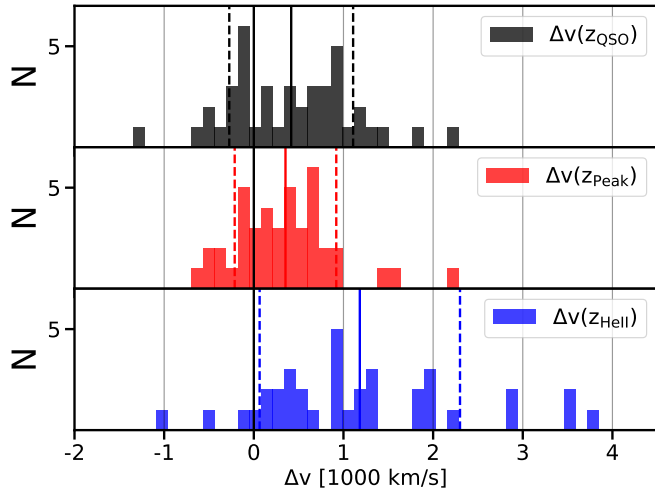


Figure 9. Distributions of CGM Ly α velocity offsets with respect to different redshifts. The top panel shows velocity with respect to the systemic (DR12Q) QSO redshift. The middle panel shows velocity with respect to the peak of Ly α emission in the QSO spectrum. The bottom panel shows velocity offset with respect to the HeII λ 1640 redshift from SDSS.

the average of giant nebulae, and the values reported in A18. There is a stark contrast between the peak value of $\sim 50\%$ for the sample-wide average and the near unity covering factor reported by A18. Even among the subset of large nebulae, the covering factor does not exceed 60%. We discuss these findings further in Section 7.

6.3. 2D Kinematic (Moment) Maps

The second column from the left in Figure 4 shows 2D Ly α velocity (first wavelength moment) maps, generated as discussed in Section 5. The majority of velocities fall within $\pm 300 - 400 \text{ km s}^{-1}$ of the flux-weighted mean velocity of each nebula. To increase clarity, velocity data is only shown for spaxels within the $\text{SNR} > 2\sigma$ contour. A number of targets exhibit instances of coherent kinematic structure on scales significantly larger than the $1 \times 1 \times 1$ (pixel) smoothing kernel used on the data. Specifically, targets 3, 5, 8, and 9 all exhibit interesting shear-like properties, with clear blue and red sides, and velocities ranging over several hundred km s^{-1} from one side to the other. The emission around target 3 in particular exhibits an unusually sharp boundary between two strongly red- and blue-shifted components in the Eastern (leftmost) half of the nebula. Targets 13, 21, and 25 also show some indications of a shear-like structure, but the area within the $\text{SNR} > 2\sigma$ contour is too small in each of them to be certain. These targets appear to be exceptions among the detections in this

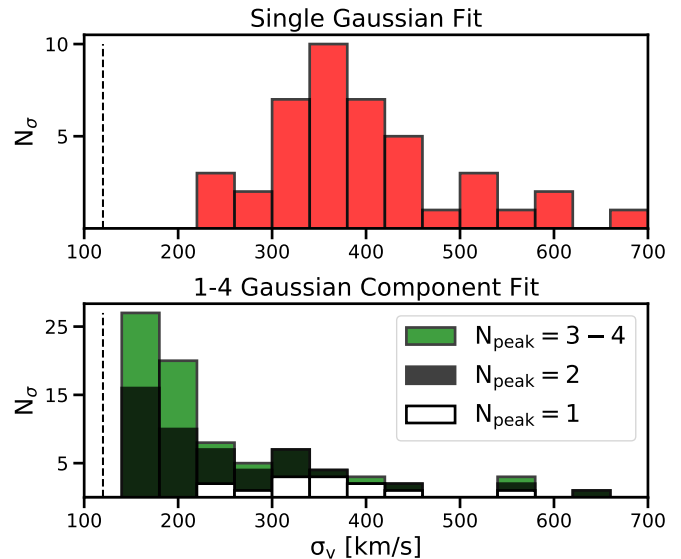


Figure 10. Top panel: global dispersions of the detected nebulae as measured from a single-component Gaussian fit. Bottom panel: dispersions of individual features when fitting spectra with a composite model of 1-4 Gaussian components.

regard, in that the remaining 35 show no clear signs of coherent structure. This is at least in part due to the small size of many of the nebulae being unable to provide a clear spatial distribution of kinematic components.

The third column from the left in Figure 4 shows two-dimensional maps of the second wavelength/velocity moment (i.e. velocity dispersion). What appears immediately obvious is that the average dispersions of the nebulae vary significantly, over a range of $\sim 200 - 400 \text{ km s}^{-1}$. Within the individual nebulae it is difficult to recognize any clear patterns, although as with the velocity maps there are instances of coherence over scales larger than the smoothing kernel (e.g. targets 2, 8). It is worth repeating here (as discussed in Section 5) that these dispersions are upper limits and are influenced by the size of the wavelength window used to calculate them. To obtain more accurate dispersion maps, deep observations are required as they will allow line fitting techniques to be used on a spaxel-by-spaxel basis.

Figure 9 shows the distributions of three velocity offsets, Δv_{QSO} , Δv_{peak} and Δv_{HeII} . The distribution of velocity offsets with respect to the systemic redshift (Δv_{QSO}) is spread over a wide range, from $\Delta v_{\text{QSO}}^{\text{min}} = -1341 \text{ km s}^{-1}$ to $\Delta v_{\text{QSO}}^{\text{max}} = +2171 \text{ km s}^{-1}$ with a median of $\Delta v_{\text{QSO}}^{\text{med}} = +399 \text{ km s}^{-1}$ and a standard deviation of $\sigma(\Delta v_{\text{QSO}}) = 691 \text{ km s}^{-1}$. The distribution

of offsets with respect to the peak of Ly α emission in the QSO spectrum is slightly more concentrated, ranging from $\Delta v_{\text{peak}}^{\text{min}} = -646 \text{ km s}^{-1}$ to $\Delta v_{\text{peak}}^{\text{max}} = +2243 \text{ km s}^{-1}$ with a median value of $\Delta v_{\text{peak}}^{\text{med}} = +353 \text{ km s}^{-1}$ and a standard deviation of $\sigma(\Delta v_{\text{peak}}) = 566 \text{ km s}^{-1}$. Finally, the spread in velocity with respect to z_{HeII} is the widest of all, ranging from $\Delta v_{\text{HeII}}^{\text{min}} = -997 \text{ km s}^{-1}$ to $\Delta v_{\text{HeII}}^{\text{max}} = +3816 \text{ km s}^{-1}$ with a standard deviation of $\sigma(\Delta v_{\text{HeII}}) = 1117 \text{ km s}^{-1}$. The median of distribution is also significantly redshifted ($\Delta v_{\text{HeII}}^{\text{med}} = +942 \text{ km s}^{-1}$).

The rightmost column in Figure 4 shows the integrated nebular spectra, extracted from the data cubes by first applying the 2D emission mask and summing over the spatial axes. Fits to the data indicate that 34/42 of the profiles can be decently described by a single- or double-peaked Gaussian, with eight targets exhibiting more complex line structure. We note that, as these spectra are spatially integrated, the line shape may be a result of the superposition of spatially separated components as well as being influenced by Ly α radiative transfer within a single, unresolved emitter. Given that the global dispersion will be heavily influenced by the presence of multiple kinematic components, we present two sets of measurements in Figure 10 in order to distinguish between the extrinsic (i.e., superposition of spatially separated components) and the intrinsic (i.e., line broadening) dispersion. The former is measured as the width of single-component Gaussian fits (top panel). These dispersions range from $\sigma_v^{\text{min}} = 167 \text{ km s}^{-1}$ to $\sigma_v^{\text{max}} = 690 \text{ km s}^{-1}$, with a mean of $\sigma_v^{\text{avg}} = 383 \text{ km s}^{-1}$ and a 1σ spread in this distribution of 57 km s^{-1} . The latter is indicated by the dispersions of the individual Gaussian components wherever a multi-Gaussian (i.e. 1-4 Gaussian components) is the best-fit model. With few exceptions, these dispersions are found to be $< 400 \text{ km/s}$. The single-component dispersion and the best-fit number of peaks are presented in Table 2.

6.4. Stacked Ly α Profiles

Figure 11 shows stacked Ly α profiles of the detected CGM emission in the pilot sample, converted to rest-frame units using (i) the redshift of the CGM Ly α emission in each field ($z_{\text{Ly}\alpha}$), (ii) the redshift corresponding to the peak of Ly α emission in the QSO spectra (z_{peak}), (iii) the systemic (DR12Q) redshift of the QSO (z_{QSO}), and (iv) the redshift of HeII emission in the QSO spectrum (z_{HeII}). None of the stacked spectra show any strong indication of the classical double-peaked Ly α profile, though this could be a result of the stacking process itself. Table 4 presents the amplitude, mean and standard deviation of each stacked profile.

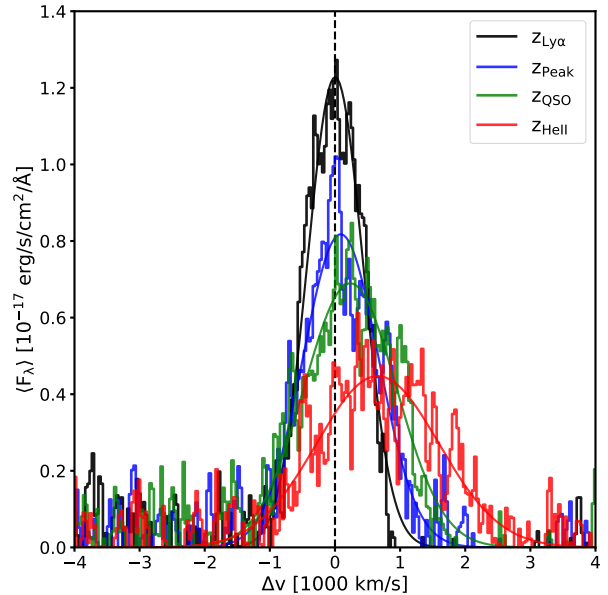


Figure 11. Stacked Ly α profiles of the CGM detections in the FLASHES pilot survey. Different colors indicate different redshifts used to convert from observed to rest-frame wavelengths: the redshift of the CGM Ly α emission itself, the redshift of the peak of Ly α emission in the QSO (blue), the QSO’s systemic redshift from DR12Q (green), and the HeII $\lambda 1640$ redshift from SDSS (red).

Table 4. Properties of Stacked Ly α Profiles

Redshift	F_{λ}^a erg s $^{-1}$ cm $^{-2}$ \AA^{-1}	v_{avg} km s $^{-1}$	σ_v km s $^{-1}$
$z_{\text{Ly}\alpha}$	1.23	-2	427
z_{peak}	0.82	+226	580
z_{QSO}	0.69	+400	709
z_{HeII}	0.45	+965	940

^aAmplitude of Gaussian fit.

With the exception of the $z_{\text{Ly}\alpha}$ -aligned profile, all of the stacked spectra -consistent with our other findings- have a clear redward bias.

7. DISCUSSION

7.1. From non-detections to Giant Ly α Nebulae

Borisova et al. (2016) report ubiquitous giant nebulae ($R_{\text{max}} \geq 50 \text{ pkpc}$) in their sample of nineteen quasars at $z \sim 3.5$. Arrigoni-Battaia et al. (2018) report ubiquitous nebulae on scales of tens to hundreds of pkpc around their sample of 61 $z \sim 3.1$ quasars. Our work reveals nebulae around 42/48 $z \simeq 2.3 - 3.1$ quasars on similar

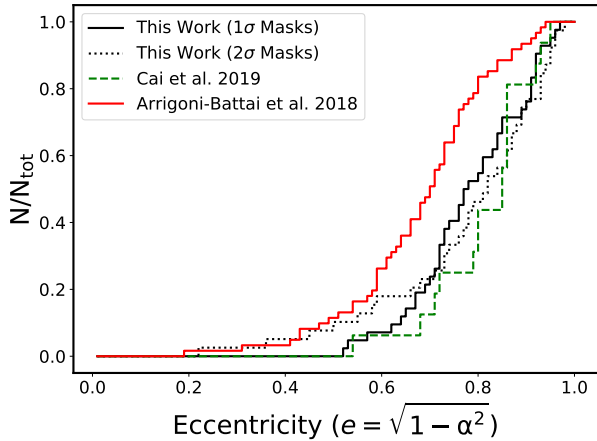


Figure 12. Cumulative distribution of nebular eccentricities for the FLASHES survey, A18 and C19. The solid black line shows the distribution as measured from the FLASHES 1σ contour object masks. The dashed black line shows those measured from 2σ contour object masks. The red line shows the distribution of values presented in A18. The green dashed line shows the distribution from C19.

spatial scales, with a few notable differences. When comparing our 2σ outer-limit object masks to A18, the nebulae we measure are smaller in R_{\max} by a wide margin (20 – 40 pkpc), shown in the bottom panel of Figure 5. Combined with the fact that our dimming-adjusted radial profiles appear to be, on average, $5\times$ fainter (with a peak brightness of $SB_{\max}^{\text{adj}} = 2 \times 10^{-15}$ compared to 10^{-14} $\text{erg s}^{-1} \text{cm}^{-2} \text{arcsec}^{-2}$), it seems clear there is a substantial difference in absolute surface brightness. However, much of this latter effect may be attributed to higher asymmetry and lower covering factors, as opposed to globally lower surface brightness values. Figure 6 shows the parameter space of luminosity and size (R_{\max}) for FLASHES compared to AB18, B16 and C19. When integrating over our 1σ object masks, the total integrated luminosities appear comparable, if even slightly brighter on average, to those in AB18, ranging from $L \sim 10^{43} - 10^{44}$ erg s^{-1} . We do not measure any luminosities in excess of $L \simeq 1.5 \times 10^{44}$ erg s^{-1} , where both A18 and B16 measure a number of very bright nebulae with luminosities of $L \gtrsim 2 \times 10^{44}$ erg s^{-1} . C19 report a few detections with luminosities close to 10^{42} erg s^{-1} . It is possible that the non-detections in our sample are similarly faint nebulae.

7.2. Asymmetry of the Ly α Emission

It is clear from visual inspection of the pNB images in Figure 4 alone that there is a pronounced degree of asymmetry in many of the detected nebulae. The distribution of values of the eccentricity parameter (e) supports this impression, with a median value of 0.78.

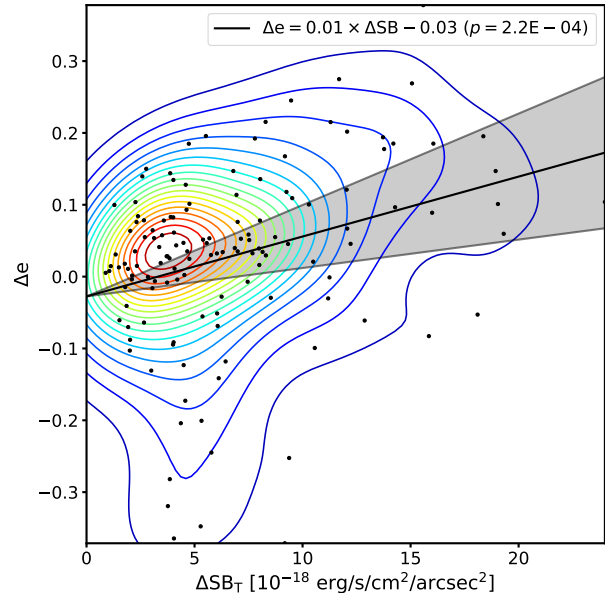


Figure 13. Change in eccentricity as a function of the increase in limiting surface brightness. Contours show a Gaussian kernel density estimate and the black line with shaded region shows the best-fit linear model with $\pm 2\sigma$ slope uncertainty. The linear regression shows a strong correlation in which eccentricity increases as the surface brightness threshold increases.

Figure 12 compares the cumulative distributions of e for the FLASHES pilot sample with those presented in C19 and A18 (none were presented in B16). To test the dependence of this comparison on our choice of initial SNR threshold, we also measure the asymmetries of detections made using the $\text{SNR} > 2\sigma$ object boundaries. We use the two-sample Kolmogorov-Smirnov (K-S) test to compare the distributions of α , and find that we can confidently reject the null hypothesis that the two samples are from the same underlying distribution when comparing to A18, regardless of the choice of mask ($p < 0.01$ - see Table 5 for exact values). Further evidence that this result is astrophysical comes from the fact that C19, using a different instrument and independent analysis, also report higher degrees of asymmetry in their $z \simeq 2.2$ sample when compared to the $z \geq 3$ MUSE studies. When comparing to C19 using the two sample K-S test, we cannot reject the null hypothesis for our 1σ - or 2σ -boundary object masks ($p \simeq 0.33$ and $p \simeq 0.48$ respectively). Table 5 summarizes the results of the K-S tests.

In addition to comparing to existing work, we test the dependence of the eccentricity parameter on the limiting surface brightness used to define the emission region within our own sample. Figure 13 shows the

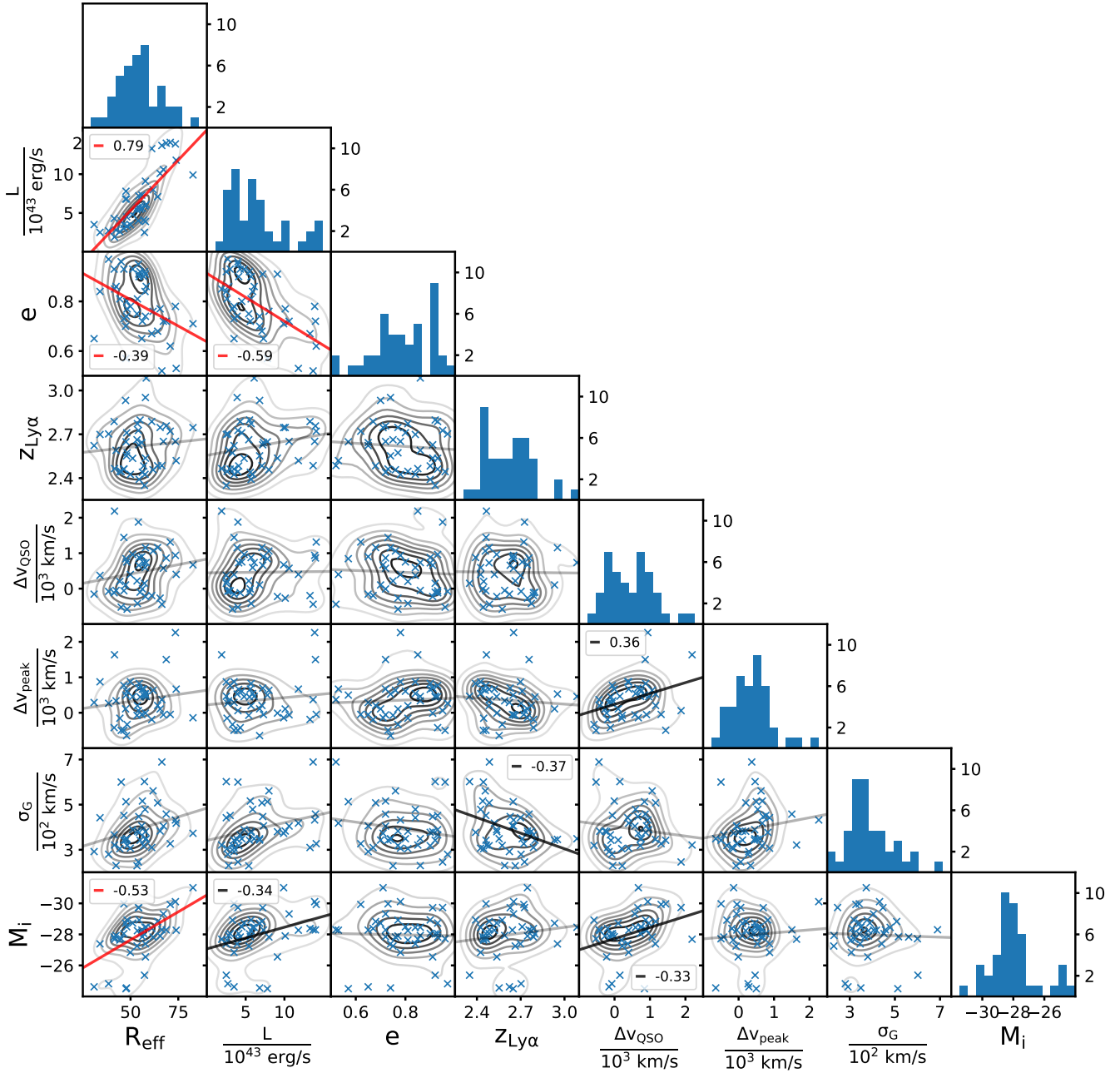


Figure 14. Parameter space plots for the nebulae detected in the FLASHES Sample. $R_{\text{eff}} = \sqrt{\text{Area}/\pi}$ is the effective size, e is the eccentricity ($0 \leq e < 1$), $z_{\text{Ly}\alpha}$ is the redshift of the nebular Ly α emission, ΔV_{QSO} and ΔV_{peak} are the velocity offsets with respect to the systemic redshift and peak of QSO Ly α emission, respectively, σ_G is the standard deviation (in km s^{-1}) of the best-fit single-peaked Gaussian line profile, and M_i is the absolute i-band magnitude of the quasar. Contours in each plot show Gaussian Kernel Density Estimates of the 2D distribution. Black and red lines show linear regression models with $p < 0.05$ and $p < 0.01$, respectively. The r-values of these linear regressions are shown on the relevant tile. Faint grey lines indicate linear regression models with $p \geq 0.05$ (i.e., no correlation clearly indicated.)

Table 5. Comparison of Eccentricity Distributions

Test	K-S Statistic	p-value
FLASHES 1σ v. A18	0.319	9.3×10^{-3}
FLASHES 2σ v. A18	0.395	7.5×10^{-4}
FLASHES 1σ v. C19	0.274	2.9×10^{-1}
FLASHES 2σ v. C19	0.223	5.4×10^{-1}

change in eccentricity as a function of the change in limiting (cosmic dimming-adjusted) surface brightness. While there is a large amount of scatter in the relationship, there is a positive correlation on average; that is: the eccentricity increases as the region is restricted to brighter and brighter emission. This relationship can be understood if one considers a CGM composed of a few small, bright, asymmetrically distributed blobs of gas with a low filling factor, and a fainter, diffuse component filling most of the halo out to similar radii. Due to its large filling factor throughout the halo, the faint gas plays the role of balancing out the second order spatial moments and reducing the eccentricity. As the threshold is increased and this fainter component is excluded, the asymmetry (eccentricity) of the bright emission becomes more exaggerated. However, the full relationship between eccentricity and limiting surface brightness is likely to be more complicated than a single linear trend. For example, one might expect that as fainter and fainter emission is revealed, and the filamentary structure of the IGM comes into play, the eccentricity might also begin to increase, reversing the relationship discussed above. Furthermore, as the surface brightness limit is increased to a point where only a single bright feature remains, on a scale close to the instrument resolution, the morphology will begin to appear more and more circular, again reversing the above relationship. Neither of these effects appear to be at play in this sample because: (i) we are not sensitive to faint enough emission to detect large filaments and (ii) we limit the size of the smallest feature to an area of 25 square pixels, above the instrument resolution and smoothing scale.

As the Ly α emission we are observing is likely powered by ionizing emission from the QSO, both the illumination and distribution of gas play prominent roles in determining the morphology of detected nebulae. These findings thus imply that either there is a systematic difference in illumination or the distribution of CGM gas between our samples and the higher redshift MUSE samples. The asymmetry of the nebulae is most likely a

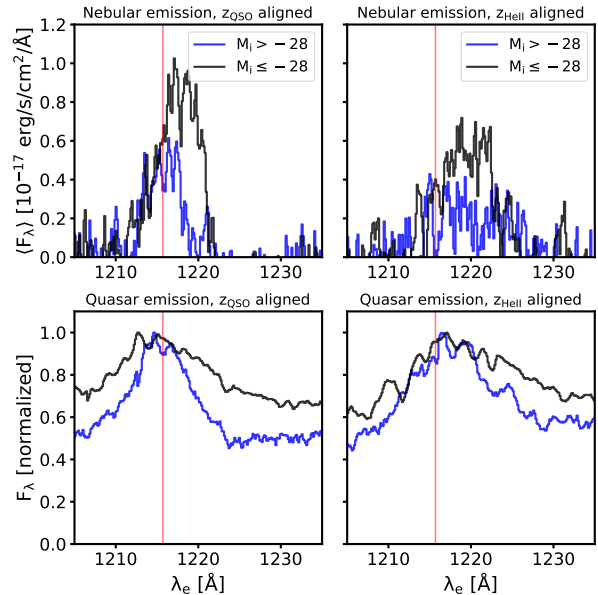


Figure 15. Stacked nebular and QSO spectra for two bins of absolute i-band magnitude (above and below $M_i = -28$), using z_{QSO} (left column) and z_{HeII} (right column) to convert to rest-frame units. Ly α from the CGM of the brightest QSOs appears to be more red-shifted than that of the fainter QSOs.

strong contribution to the low average covering factors we report, and may similarly be a result of either illumination or the intrinsic distribution of gas around the host galaxies.

7.3. Relationships between Global Nebular Properties

In Figure 14 we present a corner plot comparing some key measured properties of the detected nebulae. For each comparison, we test for any relationship between the parameters using a simple linear regression. If the result appears significant (i.e. has a p-value < 0.05) - we plot the best-fit line and show the r-value of the linear regression, indicating the strength of the correlation ($-1 \leq r \leq +1$). The strongest correlation found is no surprise - being between effective radius and luminosity. Visual inspection of this tile confirms a roughly quadratic relationship, as can be expected for these parameters. Eccentricity appears to be inversely correlated with size. Assuming size is at least in part determined by our sensitivity to faint gas throughout the halo, this is consistent with our above hypothesis that the eccentricity is reduced as fainter gas is revealed. However, we note that the overall range of eccentricities is still quite high, with the entirety of detections exhibiting values of $e > 0.5$. Eccentricity appears related to luminosity, which is another manifestation of the same relationship, given $L \propto R^2$. We find a moder-

ate correlation between the absolute i-band magnitude of the QSO, M_i , and the effective size. This appears consistent with, albeit a different representation of, the finding in AB18 of a strong correlation between the peak luminosity of the QSO and average surface brightness of detected nebulae. Similarly, we find a weak correlation between nebular luminosity and quasar magnitude.

One unexpected finding is a relationship between M_i and Δv_{QSO} , in which brighter quasars appear to have more red-shifted CGM emission on average. We investigate this phenomenon in more detail in Section 7.4. Finally, there appears to be a weak inverse correlation between redshift and the global dispersion of the integrated spectra as measured by a single Gaussian fit. This is quite surprising, especially given none of the other parameters appear to have any relationship with redshift (i.e., it cannot be easily explained through another one of the parameters such as size.) Given that the r-value is relatively small (-0.37), we will defer to the deep survey for verification and a more detailed investigation of this result.

7.4. Distributions of Ly α velocity offsets

The flux-weighted centroid of the Ly α emission measured in our sample varies by many hundreds of km s^{-1} from the systemic redshift of the QSO ($\sigma(\Delta v_z) = 691 \text{ km s}^{-1}$) and from the peak of QSO Ly α emission ($\sigma(\Delta v_{\text{peak}}) = 566 \text{ km s}^{-1}$). The spread with respect to the SDSS HeII $\lambda 1640$ redshift is even more significant, with $\sigma(\Delta v_{\text{HeII}}) = 1117 \text{ km s}^{-1}$. This spread, comparable to that reported in A18, highlights the challenge faced by narrow-band imaging searches for Ly α emission from the CGM around specific targets. All three velocity offset distributions, shown in Figure 9, present a clear bias towards the red, likely indicating re-absorption of blue-shifted emission in the intervening CGM and IGM.

Interestingly, there appears to be a weak bimodality in the distribution of Δv_{QSO} , with one peak around $\Delta v_{\text{QSO}} \simeq 0$ and another around $\Delta v_{\text{QSO}} \simeq 0$. Figure 14 shows that there is also a weak correlation between Δv_{QSO} and the absolute i-band magnitude, M_i . A closer look at the data reveals that the red-ward peak of the Δv_{QSO} distribution is attributable almost entirely to quasars with $M_i \leq -28$ mag (i.e. the brighter half of the sample). We highlight this phenomenon in Figure 15 by creating stacked nebular and QSO spectra for two bins of absolute magnitude; above and below the median value of $M_i \simeq -28$ mag. The left column shows stacked rest-frame spectra, using the systemic (DR12Q) QSO

redshift, while the right column shows the same stacked spectra, instead using the SDSS HeII $\lambda 1640$ redshift to convert to rest-frame units. When using z_{HeII} , the center of the stacked Ly α profile is at $v = +1083 \text{ km s}^{-1}$ for the CGM of the bright quasars and at $v = +681 \text{ km s}^{-1}$ for that of the fainter quasars. When stacking using z_{QSO} , the same values are $v = +419 \text{ km s}^{-1}$ and $v = -2 \text{ km s}^{-1}$, respectively. As a final test, we check if the observed correlation between Δv_{QSO} and M_i also exists for Δv_{HeII} - the velocity offset with respect to z_{HeII} . Again we find a weak correlation with r-value $r = -0.37$ and p-value $p = 0.027$; less significant but still indicative of a possible relationship between these parameters.

It is possible that this effect is a result of systematic error in the derivation of the above redshifts. For example, if the QSOs with $M_i > -28$ are mostly dust-obscured (as Figure 2 seems to imply), this may affect the spectral features of the QSOs in a way that biases the fitting process from which redshift is derived in SDSS. However, it is also possible that the local obscuring material along the line of sight is affecting both the absolute quasar magnitude and Ly α profile in a way that induces a real observed correlation, though the details of how this would work remain unclear. As the focus of the pilot survey is to present the initial insights into the CGM of these quasars, we leave a more detailed investigation of this phenomenon for a future study.

7.5. Ly α kinematics

The average dispersions of the nebulae, shown in the third column of Figure 4, appear to be in agreement with the finding of A18, in that nearly all targets have mean dispersions $\sigma_{\text{avg}} \lesssim 400 \text{ km s}^{-1}$. As we note in Section 5, the statistical second moments here provide upper limits in the presence of strong noise. However, this finding is supported by our line-fitting analysis of the integrated nebular spectra. As the top panel of Figure 10 the global dispersions of the integrated spectra have a mean of $\sigma_v = 383$ even when modelled using a single Gaussian component. In the bottom panel of the same figure, we see that the vast majority of global dispersions above 400 km s^{-1} disappear when multiple Gaussian components are allowed, indicating that these line-widths are the result of complex line shapes, attributable in part to both the superposition of spatially distinct kinematic components and intrinsically complex spectra (i.e. within a single spaxel).

One quarter (13/42) of the detected nebulae appear to be best fit by a single peak, while the plurality (21/42)

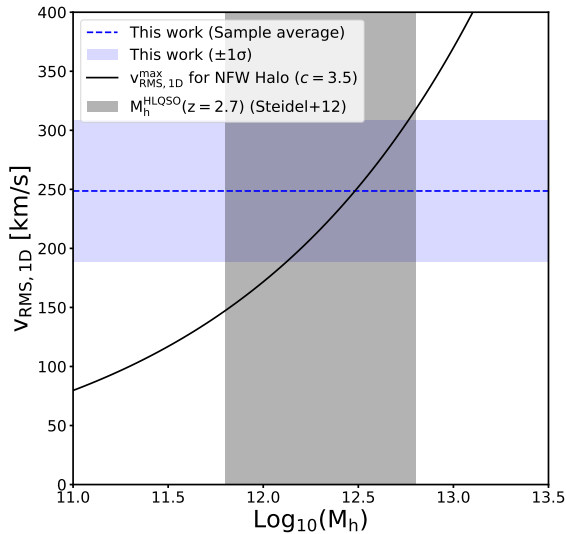


Figure 16. A comparison of the RMS line-of-sight velocity detected in the FLASHES pilot survey with gravitational motions in an NFW halo. The dashed blue line and blue shaded region represent the average and $\pm 1\sigma$ spread in the line-of-sight RMS velocities of FLASHES pilot nebulae, respectively. The solid black curve shows the (maximum) RMS line-of-sight velocity of an NFW halo as a function of halo mass following Munari et al. (2013) ($\sigma_{1D} = 0.68v_{200}$, where v_{200} is the circular velocity at the virial radius). The grey shaded region indicates the halo masses of high-luminosity QSOs (HLQSOs) at a redshift of $z = 2.7$ in Trainor & Steidel (2012b).

seem to be best described by a two-component fit, and the remaining few have more complex line shapes with three or more components. We note that these best-fit measurements, determined using the BIC, only represent the relative likelihood of the models considered, and the presence of considerable noise and occasional systematics such as bright sky-line residuals should be taken into account when interpreting these results. For example, for target 24, a bright sky line (Hg $\lambda 4358.3$) coincided almost exactly with the position of the redshifted Ly α line. A small wavelength region around this line had to be masked before analyzing the data, so the line complexity here is likely artificial.

In agreement with AB18, we find these dispersions to be consistent with values expected for gas in massive dark matter halos of mass $M_h \simeq 10^{12.5} M_\odot$. We provide a more detailed comparison of the gas kinematics in Figure 16. The solid black curve shows the line-of-sight RMS velocity ($v_{RMS,1D}$) for a Navarro-Frenk-White (NFW) halo (Navarro et al. 1997), with

a concentration parameter $c = 3.5$, as a function of halo mass. We measure the RMS velocity of each nebula detected in the sample and find the average value to be $v_{RMS,avg} = 249 \pm 60 \text{ km s}^{-1}$, which corresponds to the values expected from a halo mass range of $\text{Log}_{10}(M_h[M_\odot]) = 12.5^{+0.3}_{-0.4}$. Trainor & Steidel (2012b) measured the halo masses for a sample of high-luminosity QSOs at a redshift of $z \simeq 2.7$, and found the range to be $\text{Log}_{10}(M_h[M_\odot]) = 12.3 \pm 0.5$. The median redshift of the FLASHES sample is $z = 2.631$. We thus find that the distribution of RMS velocity values among the FLASHES pilot detections is consistent with gravitational motions expected in the host dark matter halos of QSOs at this redshift. This does not imply that such motions are the only explanation for the observed velocities, as outflows, mergers and radiative transfer may also influence kinematics. It does, however, indicate that no invocation of Ly α radiative transfer is required to explain the observations.

8. CONCLUSIONS

We have conducted the first large IFS survey targeting the $z = 2.3 - 3.1$ CGM in emission. We observed 48 quasar fields over a four-year period using PCWI on the Hale 5m telescope at Palomar Observatory. We find that:

- I Of the 48 quasars observed, 42 exhibit extended Ly α emission on a wide range of scales, varying in flux-weighted radius over $R_{rms} = 21 - 71 \text{ pkpc}$ and in maximum (radial) extent over $R_{max} = 49 - 161 \text{ pkpc}$. The average flux-weighted projected radius of the nebulae is $R_{rms}^{avg} = 39 \text{ pkpc}$ and the spread in the distribution of these sizes is $\sigma(R_{rms}) = 18 \text{ pkpc}$.
- II The circularly averaged radial profiles peak at $SB_{max}^{obs} = 1 \times 10^{-17} \text{ erg s}^{-1} \text{ cm}^{-2} \text{ arcsec}^{-2}$ in observed surface brightness and $SB_{max}^{adj} = 2 \times 10^{-15} \text{ erg s}^{-1} \text{ cm}^{-2} \text{ arcsec}^{-2}$ when adjusted for cosmological surface brightness dimming.
- III The emission appears to be similar in maximum extent (i.e., comparing R_{max}) but fainter on average than those reported in B16 or A18, with the peak of the circularly averaged radial profiles a factor of 5 lower in peak surface brightness. When restricting our object masks to 2σ outer-limits, the nebulae appear to be smaller than those in AB18 or BS16 by about $\Delta R_{max} \sim 30 \text{ pkpc}$, and the same size as those in C19.
- IV The integrated nebular luminosities range from $L_{min} = 1.9 \times 10^{43} \text{ erg s}^{-1}$ to $L_{max} = 14.1 \times 10^{43} \text{ erg s}^{-1}$

V The nebulae are highly asymmetric, with measured eccentricities ranging from $e = 0.52$ to $e = 0.97$, and a sample-wide mean eccentricity of $e_{avg} = 0.79$. Using the two-sample K-S test, we find that these nebulae exhibit distinctly higher asymmetry than those found around $z \gtrsim 3$ quasars (B16 and A18), yet may possibly reflect the same underlying distribution as those reported in C19.

VI The covering factor profiles defined by a $S/N \geq 2\sigma$ threshold in surface brightness peak at $f_c \simeq 50\%$ at small radii for the sample-wide average, and $f_{c,giant} \simeq 60\%$ for the subset of giant nebulae, which is significantly lower than those reported by A18.

VII The flux-weighted average velocity of the nebulae varies by thousands of km s^{-1} with respect to the systemic QSO redshift ($\sigma(\Delta v_{\text{QSO}}) = 691 \text{ km s}^{-1}$) and has a red-shifted bias ($\Delta v_{\text{QSO,med}} = +399 \text{ km s}^{-1}$). The flux-weighted average velocity of the nebulae also varies significantly with respect to the Ly α peak of the QSO spectrum, albeit by a smaller but considerable amount ($\sigma(\Delta v_{\text{peak}})$) and has a lesser but still red-shifted bias ($\Delta v_{\text{peak,med}} = +353 \text{ km s}^{-1}$).

VIII Most of the integrated nebular emission line profiles are either single-peaked (13/42) or double-peaked (21/42) with a few nebulae exhibiting more complex line shapes.

IX Global dispersions for the nebulae range from 167 – 690 km/s , with a mean of 383 km s^{-1} and standard deviation of 107 km/s . The average RMS line-of-sight velocity is found to be $v_{\text{RMS,avg}} = 249 \pm 60 \text{ km s}^{-1}$, consistent with that expected from QSO host halos with a mass range of $\text{Log}_{10}(M_{\text{h}}[M_{\odot}]) = 12.5^{+0.3}_{-0.4}$.

9. ACKNOWLEDGEMENTS

This work was supported by the National Science Foundation (NSF Award Number 1716907). The authors would like to thank Chuck Steidel (California Institute of Technology) and Ryan Trainor (Franklin & Marshall College) for their insightful discussions and help with target selection, as well as Sebastiano Cantalupo (ETH Zürich). We would also like to thank the staff at Palomar Observatory, for their continuous support over nearly seventy nights of observations since 2014.

REFERENCES

- Alam, S., & et al. 2015, ApJS, 219, 12, doi: [10.1088/0067-0049/219/1/12](https://doi.org/10.1088/0067-0049/219/1/12)
- Arrigoni-Battaia, F., Hennawi, J. F., Cantalupo, S., & Prochaska, J. X. 2016, ApJ, 829, 3, doi: [10.3847/0004-637X/829/1/3](https://doi.org/10.3847/0004-637X/829/1/3)
- Arrigoni-Battaia, F., Hennawi, J. F., Farina, E. P., et al. 2018, Monthly Notices of the Royal Astronomical Society, 482, 3162, doi: [10.1093/mnras/sty2827](https://doi.org/10.1093/mnras/sty2827)
- Bertone, S., Aguirre, A., & Schaye, J. 2013, MNRAS, 430, 3292, doi: [10.1093/mnras/stt131](https://doi.org/10.1093/mnras/stt131)
- Bertone, S., & Schaye, J. 2012, MNRAS, 419, 780, doi: [10.1111/j.1365-2966.2011.19742.x](https://doi.org/10.1111/j.1365-2966.2011.19742.x)
- Bianchi, L., Herald, J., Efremova, B., et al. 2011, Ap&SS, 335, 161, doi: [10.1007/s10509-010-0581-x](https://doi.org/10.1007/s10509-010-0581-x)
- Blumenthal, G. R., Faber, S. M., Primack, J. R., & Rees, M. J. 1984, Nature, 311, 517, doi: [10.1038/311517a0](https://doi.org/10.1038/311517a0)
- Bond, J. R., Kofman, L., & Pogosyan, D. 1996, Nature, 380, 603, doi: [10.1038/380603a0](https://doi.org/10.1038/380603a0)
- Borisova, E., Cantalupo, S., Lilly, S. J., et al. 2016, ApJ, 831, 39, doi: [10.3847/0004-637X/831/1/39](https://doi.org/10.3847/0004-637X/831/1/39)
- Bridge, C. R., Blain, A., Borys, C. J. K., et al. 2013, ApJ, 769, 91, doi: [10.1088/0004-637X/769/2/91](https://doi.org/10.1088/0004-637X/769/2/91)
- Cai, Z., Cantalupo, S., Prochaska, J. X., et al. 2019, arXiv e-prints, arXiv:1909.11098, <https://arxiv.org/abs/1909.11098>
- Caillier, P., Accardo, M., Adjali, L., et al. 2014, in Proc. SPIE, Vol. 9147, Ground-based and Airborne Instrumentation for Astronomy V, 91475K, doi: [10.1117/12.2057056](https://doi.org/10.1117/12.2057056)
- Christensen, L., Jahnke, K., Wisotzki, L., & Sánchez, S. F. 2006, A&A, 459, 717, doi: [10.1051/0004-6361:20065318](https://doi.org/10.1051/0004-6361:20065318)
- Correa, C. A., Wyithe, J. S. B., Schaye, J., & Duffy, A. R. 2015, MNRAS, 450, 1521, doi: [10.1093/mnras/stv697](https://doi.org/10.1093/mnras/stv697)
- Cutri, R. M., & et al. 2013, VizieR Online Data Catalog, 2328
- Dekel, A., Birnboim, Y., Engel, G., et al. 2009, Nature, 457, 451, doi: [10.1038/nature07648](https://doi.org/10.1038/nature07648)
- Fukugita, M., Hogan, C. J., & Peebles, P. J. E. 1998, ApJ, 503, 518, doi: [10.1086/306025](https://doi.org/10.1086/306025)
- Fumagalli, M., O’Meara, J. M., & Prochaska, J. X. 2011, Science, 334, 1245, doi: [10.1126/science.1213581](https://doi.org/10.1126/science.1213581)
- Gastaud, R. D., Popoff, F. S., & Starck, J.-L. 2002, Astronomical Society of the Pacific Conference Series, Vol. 281, An SAO-DS9-Based Widget Interface for Compressed Images, 173

- Helfand, D. J., White, R. L., & Becker, R. H. 2015, *ApJ*, 801, 26, doi: [10.1088/0004-637X/801/1/26](https://doi.org/10.1088/0004-637X/801/1/26)
- Kereš, D., Katz, N., Weinberg, D. H., & Davé, R. 2005, *MNRAS*, 363, 2, doi: [10.1111/j.1365-2966.2005.09451.x](https://doi.org/10.1111/j.1365-2966.2005.09451.x)
- Martin, D. C., Chang, D., Matuszewski, M., et al. 2014a, *ApJ*, 786, 106, doi: [10.1088/0004-637X/786/2/106](https://doi.org/10.1088/0004-637X/786/2/106)
- . 2014b, *ApJ*, 786, 107, doi: [10.1088/0004-637X/786/2/107](https://doi.org/10.1088/0004-637X/786/2/107)
- Martin, D. C., Matuszewski, M., Morrissey, P., et al. 2015, *Nature*, 524, 192, doi: [10.1038/nature14616](https://doi.org/10.1038/nature14616)
- . 2016, *ApJL*, 824, L5, doi: [10.3847/2041-8205/824/1/L5](https://doi.org/10.3847/2041-8205/824/1/L5)
- Martin, D. C., O’Sullivan, D., Matuszewski, M., et al. 2019, *Nature Astronomy*, 3, 822, doi: [10.1038/s41550-019-0791-2](https://doi.org/10.1038/s41550-019-0791-2)
- Matuszewski, M., Chang, D., Crabill, R. M., et al. 2010, in *Proc. SPIE*, Vol. 7735, Ground-based and Airborne Instrumentation for Astronomy III, 77350P, doi: [10.1117/12.856644](https://doi.org/10.1117/12.856644)
- Morrissey, P., Matuszewski, M., Martin, D. C., et al. 2018, *ApJ*, 864, 93, doi: [10.3847/1538-4357/aad597](https://doi.org/10.3847/1538-4357/aad597)
- Munari, E., Biviano, A., Borgani, S., Murante, G., & Fabjan, D. 2013, *MNRAS*, 430, 2638, doi: [10.1093/mnras/stt049](https://doi.org/10.1093/mnras/stt049)
- Navarro, J. F., Frenk, C. S., & White, S. D. M. 1997, *ApJ*, 490, 493, doi: [10.1086/304888](https://doi.org/10.1086/304888)
- Sérsic, J. L. 1963, *Boletín de la Asociación Argentina de Astronomía La Plata Argentina*, 6, 41
- Skrutskie, M. F., & et al. 2006, *AJ*, 131, 1163, doi: [10.1086/498708](https://doi.org/10.1086/498708)
- Storn, R., & Price, K. 1997, *Journal of Global Optimization*, 11, 341, doi: [10.1023/A:1008202821328](https://doi.org/10.1023/A:1008202821328)
- Trainor, R., & Steidel, C. C. 2013, *ApJL*, 775, L3, doi: [10.1088/2041-8205/775/1/L3](https://doi.org/10.1088/2041-8205/775/1/L3)
- Trainor, R. F., & Steidel, C. C. 2012a, *ApJ*, 752, 39, doi: [10.1088/0004-637X/752/1/39](https://doi.org/10.1088/0004-637X/752/1/39)
- . 2012b, *ApJ*, 752, 39, doi: [10.1088/0004-637X/752/1/39](https://doi.org/10.1088/0004-637X/752/1/39)
- Virtanen, P., Gommers, R., Oliphant, T. E., et al. 2019, arXiv e-prints, arXiv:1907.10121. <https://arxiv.org/abs/1907.10121>
- Wagenmakers, E.-J., & Farrell, S. 2004, *Psychonomic bulletin & review*, 11, 192
- Wisotzki, L., Bacon, R., Blaizot, J., et al. 2016, *A&A*, 587, A98, doi: [10.1051/0004-6361/201527384](https://doi.org/10.1051/0004-6361/201527384)

APPENDIX

A. EXTENDED PHOTOMETRY DATA FOR FLASHES TARGETS

Table 6. Multi-band Photometric Data (AB Magnitudes) for the FLASHES Pilot Sample

Target	GALEX ^a		SDSS DR12 ^b					2MASS ^c			WISE ^d				FIRST ^e
SDSS/HS	FUV	NUV	u	g	r	i	z	H	J	K	W1	W2	W3	W4	1.4GHz
1700+6416	18.99	18.77	16.74	16.05	15.94	15.84	15.77	16.64	17.53	16.80	15.70	15.49	13.88	13.09	...
0006+1614	...	22.86	19.18	18.33	18.13	18.10	17.84	15.22	16.15	15.78	18.00	17.42	16.00	15.38	...
0012+3344	...	20.81	18.97	18.32	18.27	18.26	17.97	17.37	18.18	17.46	17.74	17.40	15.61	14.53	...
0013+1630	18.93	18.33	18.26	18.17	17.93	16.93	18.22	17.55	17.26	17.14	15.74	14.83	...
0015+2927	19.31	18.15	17.99	18.01	17.90	17.23	18.29	17.46	17.59	17.38	16.01	15.46	...
0041+1925	20.95	19.86	19.70	19.50	19.32	17.22	18.20	17.70	19.34	19.18	17.35	15.46	...
0057+0346	...	20.65	18.84	18.18	18.13	18.06	17.84	17.62	17.34	16.19	15.30	...
0103+1316	17.32	16.57	16.37	16.27	16.16	17.00	18.37	17.21	16.37	16.00	14.02	13.18	...
0107+1104	21.51	20.96	20.66	20.68	20.39	15.85	16.84	16.38	19.98	20.22	16.88	15.62	...
0108+1635	18.1	17.19	17.00	16.87	16.67	16.56	16.30	14.75	13.91	...
0118+1950	19.11	18.14	17.99	18.01	17.89	16.04	17.18	16.73	17.84	17.64	16.12	15.21	...
0126+1559	19.77	19.00	18.82	18.81	18.60	16.77	18.10	17.50	18.62	18.37	16.78	15.66	...
0132+3326	19.73	19.10	19.18	19.10	18.77	18.00	18.02	17.32	15.27	...
0137+2405	24.93	22.23	21.80	21.67	22.06	16.55	17.75	17.54	20.30	20.00	16.98	15.06	...
0144+0838	18.92	18.38	18.26	18.27	18.09	18.25	17.46	15.66	14.92	...
0205+1902	18.31	17.45	17.27	17.07	16.90	16.64	17.53	16.80	16.75	16.43	14.58	13.84	...
0211+3117	19.71	19.00	18.86	18.86	18.79	17.30	18.31	17.75	18.89	18.54	16.64	15.14	...
0214+1912	18.77	17.97	17.91	17.74	17.39	16.64	17.53	16.80	16.79	16.41	14.97	13.98	...
0300+0222	...	22.04	18.63	18.04	17.95	17.89	17.61	16.64	17.53	16.80	17.50	17.13	15.43	14.45	...
0303+3838	20.52	19.24	18.96	18.87	18.70	16.64	17.53	16.80	18.44	17.98	16.17	15.26	...
0321+4132	18.16	17.22	16.75	16.59	16.31	16.64	17.53	16.80	16.08	15.71	14.31	13.59	...
0639+3819	21.43	20.36	20.34	20.09	19.69	16.64	17.53	16.80	19.18	19.33	16.92	15.32	...
0730+4340	...	22.43	20.52	19.19	19.06	19.00	18.87	16.20	17.17	16.79	18.67	18.41	16.89	15.70	...
0735+3744	20.32	18.68	18.56	18.34	18.13	17.86	17.59	15.78	15.40	...
0822+1626	19.79	19.45	18.36	17.88	17.88	17.90	17.67	16.48	17.69	16.39	17.60	17.24	15.63	14.93	...
0834+1238	18.95	18.17	18.02	17.94	17.82	17.09	18.00	17.34	17.78	17.40	15.49	14.28	...
0837+1459	18.4	17.74	17.74	17.72	17.44	17.24	16.86	15.17	14.41	...
0851+3148	22.58	21.32	21.64	21.60	21.47	15.46	16.68	15.82	20.66	18.96	14.97	13.41	...
0958+4703	20.99	21.63	18.5	17.73	17.73	17.65	17.35	17.31	17.19	15.88	14.84	...
1002+2008	20.01	19.09	18.94	18.85	18.64	18.50	18.16	15.29	13.31	...
1011+2941	16.76	16.17	16.09	16.02	15.90	15.87	15.64	14.21	13.45	...
1112+1521	19.58	18.10	17.96	17.82	17.58	17.23	17.09	16.43	15.12	...

Table 6 continued

Table 6 (continued)

Target	GALEX ^a		SDSS DR12 ^b					2MASS ^c			WISE ^d				FIRST ^e
SDSS/HS	FUV	NUV	u	g	r	i	z	H	J	K	W1	W2	W3	W4	1.4GHz
1218+2414	17.46	16.91	16.97	16.94	16.72	16.34	17.68	16.51	16.70	16.40	14.59	13.85	...
1258+2123	22.27	21.15	21.33	21.50	20.88	20.54	19.46	15.81	14.54	...
1428+2336	20.11	18.82	18.58	18.44	18.39	16.78	17.82	16.87	18.26	17.86	16.06	15.22	...
1532+3059	17.9	17.25	17.17	17.14	16.98	16.86	16.55	15.20	14.61	...
1552+1757	23.78	21.55	21.31	21.31	20.76	15.28	16.26	15.73	19.06	19.03	17.58	15.19	...
1625+4858	...	22.18	19.52	18.09	17.94	17.63	17.41	15.79	16.57	16.15	17.25	17.11	15.94	15.32	12.86
1625+4858	...	22.18	19.52	18.09	17.94	17.63	17.41	15.79	16.57	16.15	17.25	17.11	15.94	15.32	12.86
2151+0921	18.96	18.42	18.38	18.36	18.10	16.77	17.67	17.47	18.21	18.01	16.77	15.38	...
2234+2637	23.59	22.03	21.50	21.00	20.41	16.04	17.17	16.18	20.35	20.21	16.87	15.59	...
2241+1225	18.73	18.05	17.93	17.84	17.70	17.60	17.19	15.53	15.05	...
2259+2326	19.02	18.26	18.11	17.99	17.65	17.33	16.96	15.40	14.49	...
2328+0443	22.67	20.78	21.14	21.55	20.76	16.26	17.33	16.83	19.99	19.17	16.00	14.66	...
2338+1504	21.3	21.66	18.19	17.68	17.63	17.50	17.22	16.99	16.69	15.49	14.98	12.27
2339+1901	...	22.3	18.12	17.20	17.12	17.00	16.59	16.64	17.53	16.80	16.04	15.89	14.96	14.24	...
2340+2418	21.13	20.69	20.56	20.53	20.09	16.90	18.02	16.91	19.71	20.07	17.05	14.98	...
2350+3135	22.94	21.02	20.67	20.82	20.65	19.92	20.56	17.34	15.33	...

^aGALEX DR5 (Bianchi et al. 2011)^bSDSS DR12 (Alam & et al. 2015)^c2MASS Catalog (Skrutskie & et al. 2006)^dAllWISE Catalog (Cutri & et al. 2013)^eFIRST Survey

B. CLOSING WINDOW CALCULATION

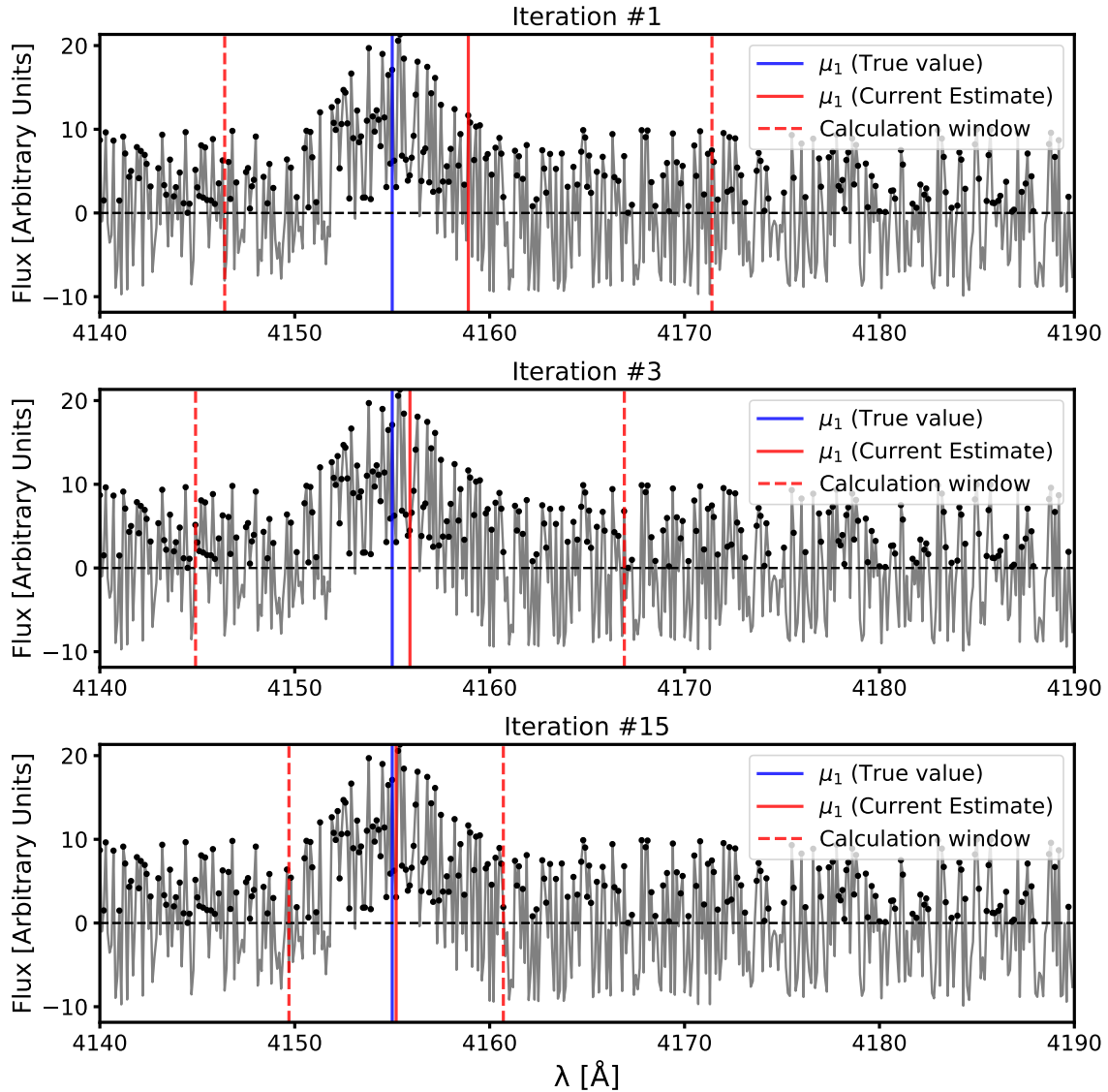


Figure 17. The iterative method, called the 'closing-window' method, used to calculate the first moments of noisy spectra. Each panel shows the noisy spectrum in grey, with positive values shown as black points. The vertical blue line indicates the true first moment of the simulated signal. From top to bottom, the panels show the estimate of the first moment for the 1st, 3rd and final iterations, respectively. The vertical red lines show the size of the window used to perform the calculation. The window size starts at 25\AA in order to explore the full range of the pNB bandwidth. Upon each iteration, the window center is updated to the most recently calculated value of μ_1 , and the window size is decreased by $\Delta\lambda = 1\text{\AA}$ until a minimum size of 10\AA is achieved. The shrinking window size helps to mitigate the influence of noise on the calculation, while the iterative process allows the calculation to converge on the true value.